反応焼結法による希土類単硫化物 RESx　(RE = Gd, Ho)の合成

Synthesis of rare-earth monosulfide RES_x (RE = Gd, Ho) compacts by reaction sintering

反応焼結法による希土類単硫化物 RES_x (RE = Gd, Ho の合成)

Dissertation

Submitted to Muroran Institute of Technology
Division of Production Systems Engineering
In Partial Fulfillment of the Requirements
For the Degree of Doctor of Engineering

By

Tran Nhu Bien

Muroran Institute of Technology,
Muroran, Hokkaido, Japan

December 2020

Certificate of Approval

This dissertation entitled:

Synthesis of rare-earth monosulfide RES_x (RE = Gd, Ho) compacts by reaction sintering
反応焼結法による希土類単硫化物 RES_x (RE = Gd, Ho の合成)

Written by Tran Nhu Bien
has been approved for the Division of Production Systems Engineering
Muroran Institute of Technology, Hokkaido, Japan

Date: Professor Dr. Shinji Hirai

Professor Dr. Chihiro Sekine

Signed by the final examining committee:

– Professor Dr. Isao Saeki

– Professor Dr. Chihiro Sekine

– Professor Dr. Toshihiro Kuzuya

The final copy of this dissertation has been examined by the signatories, and we find that both the content and form meet acceptable presentation standards of scholarly work in the above-mentioned discipline.

Dedication

To my supervisor

To my family

To my wife

Acknowledgments

I extend my deepest gratitude to my supervisor, Prof. Hirai Shinji. His support and encouragement during my time as a Ph.D. student was invaluable and very important. I would like to express my deepest thanks to Prof. Sekine, my co-supervisor, who was always most helpful when called upon. During the medical leave of Prof. Hirai Shinji, special advisor Dr. Kazuhei Wakiya stood in as superintendent, and I would like to express my gratitude for his guidance and suggestions. I would also like to thank Prof. Saeki, Prof. Kamegawa Atsunori, Prof. Toshihiro Kuzuya, and Dr. Kawamura for their valuable comments and instructions.

I would like to express my sincere thanks to Prof. Inga Vasilyeva and Dr. Ruslan Nikolaev from the Nikolaev Institute of Inorganic Chemistry (Russian) for their support in terms of melting-point measurements, quick responses to all my requests, and for reviewing my article. Prof. Vitalij K. Pecharsky and Prof. Arjun K. Pathak are likewise acknowledged for supporting me during my internship at Ames Lab and for their suggestions for my studies.

I am fortunate to have fantastic friends, lab mates, colleagues, and a research team, including Hoang Anh Tuan, Mohammed Alharbi, and Akie Kuroda; I deeply appreciate our talks and discussions, work-related or otherwise. I would also like to thank all my friends and my laboratory staff for all the precious help during my studies at the Muroran Institute of Technology.

Last but not least, my appreciation also goes out to my family, my parents for their endless love, care, and encouragement throughout my life and my studies in Japan, and to my younger sister for always letting me know how proud she is of me. Lastly, I would like to express my gratitude to my wife and my children for always being there for me. Without their tremendous understanding and encouragement over the past few years, it would have been impossible for me to complete my studies.

Abstract

Rare-earth monosulfides, or RES (RE = Gd, Ho), have attracted significant attention because of their potential application as cathodes in organic light emitting diodes, thermal-expansion compensators, thermoelectric generators, and magnetic recording and electronic devices. However, the synthesis of pure RES is still challenging because the RE metal, as a raw material, is easily oxidized and the current synthesis methods are complex. This study examined simple synthesis methods for obtaining high-purity RES. Stoichiometric and non-stoichiometric GdS_x and HoS_x ($0.68 \leq x \leq 1.2$) were synthesized by the direct reaction sintering of α-Gd_2S_3 and GdH_2 for GdS_x and δ-Ho_2S_3 and Ho metal for HoS using a pulse electric current sintering apparatus.

The synthesized compacts were characterized by microscopic analysis using an X-ray diffractometer, EDX analyzer, and an O/N/H analyzer. The X-ray diffraction results showed that GdS_x and HoS_x sintering compacts can be obtained without an impurity phase by optimizing the sintering temperature. The actual composition for the GdS_x and HoS_x sintering compacts can be varied from $GdS_{1.10}$ to $GdS_{0.75}$ and $HoS_{1.19}$ to $HoS_{0.83}$, respectively. The study revealed that the rare-earth and sulfur defects arising from rare-earth additions within the homogeneity range strongly affect the lattice parameter, melting point, and electrical resistivity. The resistivity of the stoichiometric compound shows a metallic behavior down to several Kelvin, while in the off-stoichiometric compounds, semiconductor-like behavior appears below the magnetic ordering temperature. The lattice parameter and the melting point become the highest when the composition is close to stoichiometric. These insights about the synthesis process and the relation between composition and properties provide guidelines for further general problem solving in O-free RES preparation.

概要

希土類単硫化物は NaCl 型の結晶構造をもち，光学デバイス，太陽電池，フォトダイオード，磁気記録デバイスなどのエレクトロニクス分野における応用に不可欠な材料である。しかし，希土類金属と硫黄の蒸気圧が大きく異なる点，単体の希土類金属が極めて酸化しやすい点，これまでの試料作製方法が非常に多くの反応プロセスを伴う複雑なものであることなどから，純良な希土類単硫化物試料の合成は困難であった。本研究では，これまで研究例のほとんどない，Gd, Ho を含む希土類単硫化物に着目し，CS_2 ガス硫化法により作製した希土類三二硫化物（α-Gd_2S_3, δ-Ho_2S_3）と希土類単体（Ho）もしくは希土類水素化物（GdH_2）を出発物質とし，放電プラズマ焼結（SPS）装置を用いた反応焼結法により，物性測定が可能である大きなサイズの希土類単硫化物 GdS, HoS の純良な単一相焼結体の合成に成功した。また，出発原料の希土類と硫黄の比率を変えることにより，非化学量論比組成の GdS_x，HoS_x の単一相焼結体を広い組成範囲で合成することにも成功した。さらに，得られた試料について，結晶構造解析，元素組成分析，微量に含まれる不純物の同定を行い，熱物性，電子物性を詳細に調べた。その結果，格子定数，融点，電気伝導率の変化が，希土類と硫黄の組成比（x）と密接に関係していることを確認した。

本研究では，従来の方法よりも単純なプロセスで不純物の少ない純良な希土類単硫化物の大型焼結体の合成が可能であることを示した。さらに，出発原料の比率を変えることで，非化学量論比組成の希土類単硫化物における希土類と硫黄の組成比（x）を制御することが可能であることを示した。さらに，希土類と硫黄の組成比（x）を変えることで電気伝導率などの物性を大きく変化させることが可能であることから，今回得られた結果は，物性値の最適化を行う上でも重要な知見であると考えられる。これらの結果は，Gd, Ho 以外の希土類単硫化物にも応用が可能であると考えられ，今後の希土類単硫化物の設計の幅を広げることにつながり，次世代の高性能デバイスに不可欠な材料開発の発展に寄与するものであると考えられる。

Contents

List of Figures

List of Tables

Chapter 1 Introduction

1.1 Rare-earth monosulfides

The rare-earth monosulfides (RES) form–the cubic NaCl-type structure as shown Figure 1 [1]. They have attracted much attention because of their potential use as a cathode in organic light emitting diodes [2], [3], thermal-expansion compensators [4], thermoelectric generators, magnetic recording and electronic devices [5], and magnetic refrigerants [6]. Magnetic measurements of RES showed that most rare-earth (RE) atoms are trivalent, meaning that an unbonded electron, $Ln^{3+}(e^{-})S^{2-}$, is present. The extra electron is delocalized in the 5d conduction band, resulting in the metallic-type conduction. In contrast, EuS, SmS, and YbS contain divalent RE atoms, thus, there are no extra electrons, and these compounds behave as semiconductors or semimetals [1]. The following section provides a brief review of RES.

1.1.1 CeS

CeS has a high melting point, low vapor pressure, low chemical reactivity with molten metals, and other characteristics which make it suitable for refractory materials. The change in free energy during the formation of CeS has a larger negative value than that for Ce_2S_3. This may account for the chemical inertness of CeS toward many molten metals. Additionally, CeS possesses outstanding conducting properties. The electrical resistivity is as low as 0.72×10^{-4} Ω·cm at 293

K and 1.12×10^{-4} Ω·cm at 1273 K. In contrast, the thermal conductivity is as low as 39 $W/(mK)^{-1}$, which is comparable to alumina. Because of these conducting properties, CeS is a potential candidate to be applied in induction heating.

1.1.2 SmS

SmS has received extensive attention because it shows a pressure-induced transition from the semiconducting to the metallic state [7], [8]. The semiconducting–metallic transition is driven by the variable oxidation state of Sm. Samarium has two possible ground state configurations in SmS, including the nonmagnetic Sm^{2+} with the $4f^6(^7F0)$ configuration and the magnetic Sm^{3+} with the $4f^5(^6H_{5/2})$ configuration [9]. The Sm valence state changes from a predominantly 2+ state (black, semiconducting state) to a mainly 3+ state (golden, metallic state). Consequently, the color of SmS is changed by the transition, earning it the name of the black–golden transition. The importance and uniqueness of this material is based on its switching characteristics driven by pressure. For other switchable materials, such as VO_2, the switching requires proper heating/cooling cycles [5]. Furthermore, other studies of SmS showed the applicability of this material in high-quality sensing and memory devices, as well as very presumably in optical switching devices, due to the laser-induced transition of SmS [10]–[12].

1.1.3 EuS

EuS shows a ferromagnetic transition at 16.2 K. EuS has attracted interest as model crystals for the investigation of ferromagnetism in semiconductors [13]. The dominant exchange interaction is among the nearest neighbor Eu^{2+} ions [14]. Europium shows a large magnetic entropy change at approximately the ferromagnetic transition temperature. Therefore, EuS has potential application in magnetic refrigerant materials [6], [15].

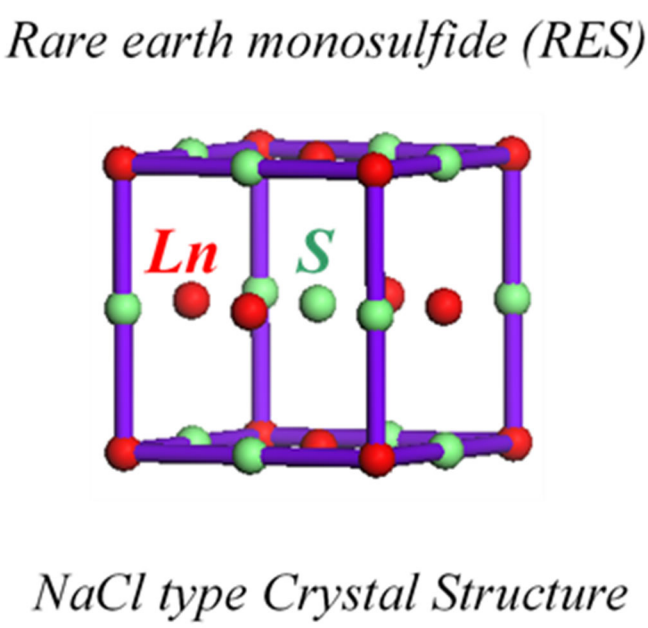

Figure 1.1 Crystal structure of RES (RE: Rare-earth)

1.1.3 GdS and HoS

GdS is an antiferromagnetic with an approximate Néel temperature of 60 K. Any increase in the sulfur content up to Gd_3S_4 or Gd_2S_3 may lead to a structural transition to the Th_3P_4-type and the appearance of the ferromagnetic order. In contrast, excess Gd generates an antiferromagnetic–ferromagnetic transition in adjunction with a semiconductor–metal transition [16]–[18]. Therefore, pure GdS (and that with added Gd) has actual and potential applications in the electronics fields, such as optical devices, photovoltaics, photodiodes, and magnetic recording devices [18]. GdS easily forms defects that affect the physical and chemical properties. Vasilev and Beckenbaug reported that the electrical conductivity is strongly dependent on sulfur vacancies [19], [20].

HoS also crystallizes with the cubic NaCl type-structure. Neutron diffraction measurements showed that HoS exhibits a Type-II antiferromagnetic order at the Néel temperature of $T_N = 21$ K [21]–[23]. HoS has been widely studied because of its intriguing physical properties and potential applications in electronic and magnetic recording devices [15], [24]–[27]. Furthermore, HoS possesses a large specific heat, close to the liquid H temperature, hence, it is expected to be applied to cryopanels close to this temperature.

As mentioned above, GdS and HoS possess intriguing properties. However, the practical application of the RES (GdS and HoS in particular) has not yet been consistent with its inherent ability. This may be because they are difficult to prepare

as they require clean stoichiometric crystals. Therefore, caution is recommended when interpreting results that could be sensitive to the sample quality. However, no previous literature exists on the effects of impurities, such as O, on the chemical and physical properties of RES.

1.2 Review of the synthesis of rare-earth sulfides

This section briefly reviews the various methods used to synthesize RES.

1.2.1 Direct reaction of elements

RES can be obtained from a direct reaction between rare-earth elements and sulfur vapor. In this method, 0.5–1.0 mm-thick slices of RE metals are reacted in sulfur vapor where the temperature is progressively raised to 1050 °C and maintained for two or three days. The product is crushed, pressed in an agate mortar, and re-sintered for two or three days. To obtain solid samples, the sample are sealed under vacuum in a tantalum crucible, and the temperature is maintained at slightly higher than the melting point, and thereafter cooled down to room temperature within 30–60 min [28].

Alanko *et al.* reported another method in which RE elements and mechanochemical processes were used [29], where the driving force for the chemical reactions was partially supplied by energetic milling media impacts. In a typical synthesis, 5 g of the rare-earth ingots and sulfur powder were milled in an argon atmosphere glovebox with PO_2 < 30 ppm. Two milling media sizes (5– and 10–mm diameter) were used to help randomize the media trajectories and increase the contact area with the vessel interior during milling. The milling was conducted at 500 rpm for between 50 min and 12 h. However, a small amount of RE_2S was detected as an impurity.

1.2.2 EuS

EuS is a special case because it can be directly obtained by the action of an H_2S stream on Eu_2O_3 contained in a graphite crucible at 1100–1200 ºC [30]. The action of an H_2S stream on the oxalate [31] or on the sulfate [32] was also used.

In contrast, our research group synthesized EuS by reacting CS_2 gas and Eu_2O_3 powders [33] and obtained single-phase EuS powders at 800 °C for 8 h.

1.2.3 Reaction of the RE metals on RE_2S_3 sulfides

CeS

Eastman *et al*. used this method first used synthesize CeS powders [34]. A mixture of Ce_2S_3 and CeH_3 was heated to approximately 400 °C to dissociate the hydride and form powdered Ce metal, followed by heating the sample to 2000 °C in a vacuum.

In contrast, Hirai *et al*. found that CeS powders can be synthesized by reacting Ce_2S_3 powder with Ce metal using a spark plasma sintering apparatus at 1273 K for 10.8 ks [15]. In this method, Ce_2S_3 was obtained from the CS_2-gas sulfurization of ceria (CeO_2) powder [19]. The synthetic CeS powders contained a small amount of Ce, Ce_2O_2S, and β-Ce_2S_3 as impurities [15]. However, for the CeS sintered compact prepared by spark plasma sintering, the O content gradually decreased as the

sintering temperature increased due to evaporation of the volatile CeO [15]. Single-phase CeS compact was formed by sintering at 2173 K [15]. To evaluate the activation energy for the densification of CeS, a CeS powder was prepared by milling an initial sintered compact and utilizing it as an ingredient for hot-press sintering experiments [15]. The densification data during hot-press sintering was analyzed using a kinetic equation and the analysis showed that boundary diffusion was the rate-limiting process, as similarly reported for the sintering of Ce_2S_3, SiC, and Al_2O_3 [15]. This result suggests that the boundary diffusion model can explain the densification data with an apparent activation energy of 479 $kJ \cdot mol^{-1}$ [15].

The direct action of RE metals on RE_2S_3 were also used for all RES powders (except for EuS, TmS, and YbS) [35]. The advantage of this method is the formation of homogeneity ranges with low S contents from the RES powders. In this method, the mixtures of metal and RE_2S_3 were heated to approximately 1350 °C in a Ti boride vessel. The use of graphite vessels must be avoided to prevent the formation of RE carbides. For the stoichiometric composition, the reaction proceeded for only 1 h. In contrast, for the various non-compositions, raw materials were thermally heated for several hours to obtain homogeneous phases [35].

1.2.4 Synthesis of RES (RE = Gd, Ho)

Several applicable reports, among the RE sulfides literature, exist concerning the GdS and HoS synthesis methods.

The synthesis of pure GdS remains a challenge because Gd, as a raw material, is easily oxidized. Therefore, sharp distinctions between the thermodynamic properties of Gd and S (melting and boiling points) and the low kinetics of their interaction generate a spatial chemical inhomogeneity. Additionally, the considerable Gd affinity to O leads to undesired oxidized by-products that are difficult to detect if they are miniscule. Therefore, in most synthesis methods, Gd_2S_3 is used as the starting material to reduce the effect of oxidation. Because both α-Gd_2S_3 and GdH_2 are stable in air at room temperature [36], [37], α-Gd_2S_3 can be prepared by sulfurization of Gd_2O_3 powder using CS_2 or H_2S gas [38], [39]. For a considerable period of time, GdS has been synthesized by reacting Al with equimolar Gd_2S_3 and Gd_2O_2S [40] according to the following reaction:

$$3Gd_2S_3 + 3Gd_2O_2S + 4Al = 12GdS + 2Al_2O_{3s} \quad (1.1)$$

To remove Al_2O_3, the product is treated by heating above 1700 ℃ for 2 h under vacuum because Al_2O_3 can be eliminated by sublimation as a volatile Al suboxide under vacuum at this temperature.

GdS has also been synthesized by using the carbothermic reduction of Gd_2O_3 [41]. After pelletizing a mixture of Gd_2S_3, soot, and Gd_2O_3 (according to the mole ratio as required by Eq.(1.2)), the mixture was vacuum heat treated at 1600 ℃ for 2–3 hours, followed by grinding, repelletization, and a final heat treatment at 1700 ℃ for 2 h. The analytical composition of the obtained GdS was 82.81% Gd and 16.59% S, and it contained 6% free carbon as an impurity.

$$Gd_2O_3 + 2Gd_2S_3 + 3C = 6GdS + 3CO \quad (1.2)$$

GdS also can be prepared by a two-stage process from metal filings and powdered S [42]. First, the reaction of Gd with excess S was conducted in a sealed evacuated fused silica tube maintained at 500 °C for several days. Next, after adding excess Gd, GdS exhibiting a gold color was obtained by heat treating it in a Knudsen cell at 900 °C for 6 h and then at 1950 °C for 24 h to eliminate the excess Gd.

Furthermore, single crystals have been grown from molten GdS [20], [43]. After pre-reacting a mixture of Gd chips and S in a sealed silica tube at 1600 °C and forming a pellet, the pellet was heated above the melting point in a Ta tube or W crucible. Then, after sufficient homogenization of the molten metal, a single crystal of GdS was grown by annealing for several hours at a temperature 20–50 °C lower than the melting point.

Moreover, GdS nanoparticles were produced in solution at ambient temperature using the ionic starting materials of $GdCl_3$ and Na_2S in the presence of dextrose [44].

HoS was synthesized from the direct reaction of elements [22], [45]. However, high purity was difficult to achieve when the Ho and S elements were used. Furthermore, it was reported that the HoS composition was difficult control [23].

1.3 Purposes

RES have been intensively studied since late last century. However, the synthesis of RES is still challenging owing to the complexity of the current synthesis methods. In particular, only some reports on the GdS and HoS synthesis methods are available. Furthermore, most RES prepared by the previously mentioned methods contain impurities and it has not been well clarified how the sample quality impacts their properties, though RES easily forms defects. Therefore, it is important to systematically study how defects affect the chemical and physical properties of RES.

In this study, a simple RES (RE = Gd or Ho) synthesis method was developed by combining the CS_2 sulfurization of RE oxides and reaction sintering with a pulse electric current sintering apparatus. The processing conditions, including the heating rate, temperature, and duration of sintering, were examined to produce single-phase and chemically homogeneous compacts.

Additionally, the effect of defects by the RE metal addition on the lattice constant, melting point, and electrical resistivity were studied. Moreover, the detailed features of the microstructure and experimental density results were considered to estimate the purity, porosity, and grain boundary state to understand the relationship between the microstructure and the macroscopic physical properties of compacts. The capabilities of the sintering process provided with highly dense compacts as a peculiar interface were also considered.

Chapter 2 Experimental

2.1 Synthesis method

GdS and HoS were synthesized by the CS_2 gas sulfurization of Ho and Gd oxides and reaction sintering with a pulsed electric current sintering apparatus (SPS).

2.1.1 CS_2 gas sulfurization

Figure 2.1 depicts a schematic diagram of the sulfurization apparatus. RE sesquisulfides (α-Gd_2S_3 and δ-Ho_2S_3) were synthesized according to reaction (2.1) [46]:

$$2Ln_2O_3 + 3CS_2 \rightarrow 2Ln_2S_3 + 3CO_2 \quad (2.1)$$

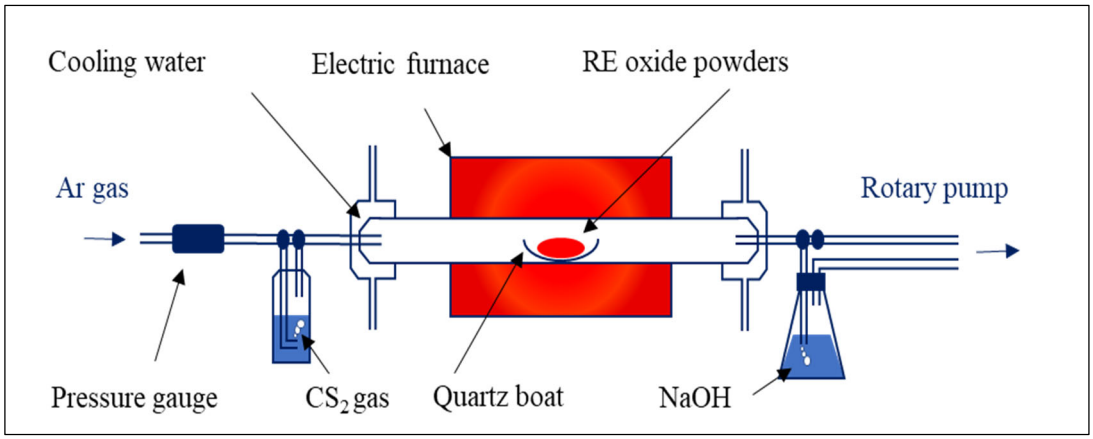

Figure 2.1 Schematics of the experiment apparatus used for sulfurization reaction

Gd_2O_3 powder (99.99%, Shin-Etsu Chemical Co., Ltd., Tokyo, Japan) with a 2.2354 μm mean particle size was placed in a quartz boat and inserted into a silica glass tube. After flushing with Ar gas at room temperature, the boat was heated to 1273 K before the Ar gas was replaced by CS_2 gas. The CS_2 gas was introduced into the reaction tube by passing the Ar carrier gas through a bubbler that contained reagent grade liquid CS_2. The flow rate of Ar gas was fixed at 80 mL/min. After being held at this temperature for 2 h, the boat was gradually cooled to room temperature under an Ar atmosphere.

For the synthesis of δ-Ho_2S_3, Ho_2O_3 powder with an average 1.6 μm particle size (99.99%, Shin-Etsu Chemical Co., Ltd., Fukui, Japan) was used as a starting material. The sulfurization was performed under the conditions presented in Ref. [47].

2.1.2 Pulsed electric current sintering apparatus

Pulsed electric current sintering is also known as spark-plasma sintering (SPS). Figure 2.2 presents a photograph of the equipment used in this study. The SPS enables the high-speed synthesis of materials and components from metals, ceramics, polymers, and composites. The SPS is often used for the synthesis of materials that are difficult to deform by conventional pressure-less sintering or hot isostatic pressing [48]–[50]. The sintering conditions are described in Section 2.1.3.

Figure 2.2 The pulsed electric current sintering apparatus

2.1.3 RES (RE = Gd, Ho) synthesis method

Figure 2.3 presents a flowchart of the preparation process of RES (RE = Gd or Ho). The synthesis of RES (RE = Gd or Ho) is based on the direct reaction between rare-earth sesquisulfide (α-Gd_2S_3 and δ-Ho_2S_3) and gadolinium hydride (GdH_2) for α-Gd_2S_3 and Ho metal for δ-Ho_2S_3. In this study, the rare-earth sesquisulfide (α-Gd_2S_3 and δ-Ho_2S_3) was prepared by the sulfurization of a RE oxide as described in Section 2.1.1.

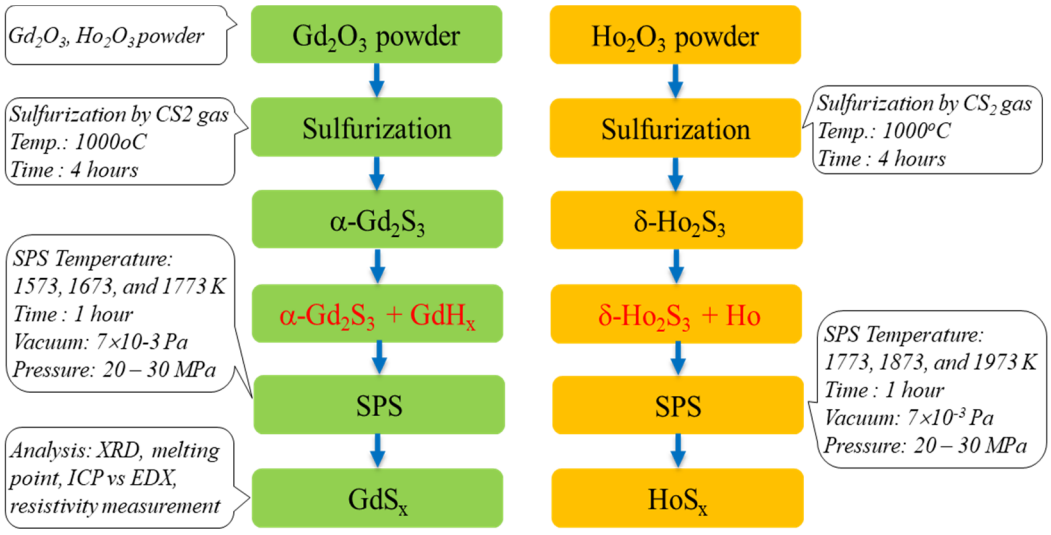

Figure 2.3 Process of synthesis of rare earth monosulfides

GdS

The α-Gd_2S_3 and GdH_2 (Kojundo Chemical Laboratory Co., Ltd) powders were mixed at the nominal compositions shown in Table 3.1 in air using an agate mortar. In this study, the preparation ratios were described as the mass percent of GdH_2 in the mixture (chemical formula calculated from the preparation ratios). Next, 3 g of the mixture was mounted in a graphite die with a 15 mm inner diameter and introduced into a SPS (SPS-511L, Sumitomo Coal Mining Co., Tokyo, Japan). The apparatus chamber was then evacuated to 7.0×10^{-3} Pa. The sintering was performed at a temperature ranging from 1373 to 1773 K for 1 h under a uniaxial pressure of 20 MPa. This sintering temperature was determined based on the isothermal potential diagrams discussed below. Both of the heating and cooling rates were fixed at 25 K/min.

Figure 2.4 shows the isothermal potential diagrams of the Gd–S–O system at 1773, 1973, and 2173 K for predicting the single-phase GdS formation state [51]. The diagrams were drawn based on data from the MALT software (Materials-oriented Little Thermodynamic Database, Kagaku Gijutsu-Sha Group, Tokyo, Japan) [52]. The diagram was taken as a base for the accurate interpretation of the phase state of the prepared compacts, especially when O-consisting impurities were present. Based on the Gd–S–O diagram, the equilibrium states at specific points and lines at 1773 K are shown by the red circles and lines in Figure 2.4 and are listed in Table 2.1.

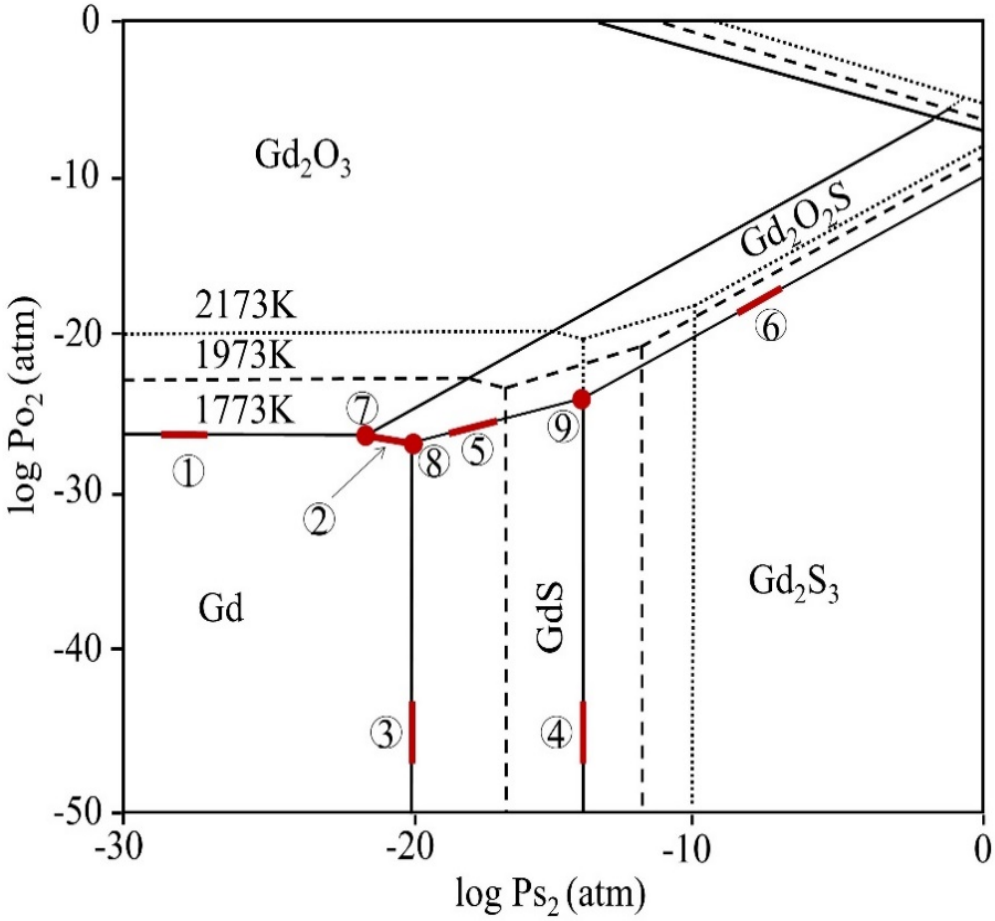

Figure 2.4 Potential diagram of Gd-O_2-S_2 system at 1773, 1973 and 2173 K

Lines 3 and 4 indicate that GdS can be formed from Gd_2S_3 by S evaporation or from gaseous Gd and S_2 species when their partial pressures are extremely low. GdS can also be formed from Gd_2S_3 without passing through a route in which Gd_2O_2S is formed if the O content of Gd_2S_3 as a raw material is sufficiently small and the S potential (log PS_2) is sufficiently low. Moreover, the log PS_2 gradually increases with increasing temperature. We also predicted that GdS can be formed from Gd_2O_2S even at a relatively high log PS_2 and O potential (log PO_2) at higher temperatures. However, the synthesis at high temperature increases the evaporation of Gd and reduces the GdS formation area; thus, the temperatures of 1373, 1573, and 1773 K were used to prepare GdS_x.

Table 2.1. Equilibriums in the Gd-S-O system at 1773 K

Line and point on diagram	**Coexisting phases**	**Reactions of the phase interaction**
Line 1	Gd, Gd_2O_3	$4Gd + 3O_2 \leftrightarrow 2Gd_2O_3$
Line 2	Gd, Gd_2O_2S	$4Gd + 2O_2 + S_2 \leftrightarrow 2Gd_2O_2S$
Line 3	Gd, GdS	$2Gd + S_2 \leftrightarrow 2GdS$
Line 4	GdS, Gd_2S_3	$2Gd_2S_3 \leftrightarrow 4GdS + S_2$
Line 5	GdS, Gd_2O_2S	$Gd_2O_2S \leftrightarrow GdS + (Gd + O_2)$
Line 6	Gd_2S_3, Gd_2O_2S	$3Gd_2O_2S \leftrightarrow Gd_2S_3 + (4Gd + 3O_2)$
Point 7	Gd, Gd_2O_3, Gd_2O_2S	$3Gd_2O_2S \leftrightarrow (2Gd + 3/2S_2) + 2Gd_2O_3$
Point 8	Gd, GdS, Gd_2O_2S	$Gd_2O_2S \leftrightarrow GdS + Gd + O_2$
Point 9	GdS, Gd_2S_3, Gd_2O_2S	$3Gd_2O_2S + 2S_2 \leftrightarrow 4GdS + Gd_2S_3 + 3O_2$

HoS

HoS_x sintered compacts were prepared by a reaction similar to that of GdS [53]. However, for the synthesis of HoS, Ho metal powder, instead of hydride, was involved in the reaction with δ-Ho_2S_3. Thus, the reaction of HoS_x ($0.68 \leq x \leq 1.2$) can be described by the following reaction (2.2):

$$xHo_2S_3 + (3-2x)\,Ho = 3HoS_x \qquad (2.2)$$

The Ho powder was prepared by grinding a Ho ingot (Kojundo Chemical Laboratory Co., Ltd.) using a diamond file. Note that the preparation of Ho powder and the mixing of δ-Ho_2S_3 and Ho powders were performed in air. A series of HoS_x samples with different initial Ho_2S_3/Ho ratios (Table 3.4) were prepared using 6 g of each mixture in a graphite die with 10 and 15 mm inner diameters, which was introduced into the SPS (SPS-511L, Sumitomo Coal Mining Co., Tokyo, Japan). Sintering was performed at the temperatures of 1773, 1873, and 1973 K for 1 h under a uniaxial pressure of 20 MPa with 7.0×10^{-3} Pa of evacuation. 5, 10, and 25 K/min heating rates were tested to find the best value for producing samples with high compactness. The sintering temperatures were chosen because of the reasons described below.

Because of the similarity with the Gd–S–O system, that was well studied in Ref. [53], it is plausible that Ho_2O_2S can appear as an impurity phase at high temperatures according to reaction (2.3). This is because O exists as the residual O

of Ho_2S_3 and a thin-surface oxidized Ho_2O_3 layer, which is universally present on the Ho particles. Furthermore, O is also present inside the sintering apparatus.

$$Ho_2S_3 + 2Ho_2O_3 = 3Ho_2O_2S \quad (2.3)$$

Both O sources clearly show that the amount of Ho_2O_2S phase depends on the thermodynamic parameters of the sintering process, on the amount of added Ho, and the thickness of the Ho oxidized layer. Thus, sintering temperatures of approximately 2000 K were desirable for this study because of the detectable vaporization of Ho_2O_3, as in the case of other RE oxides that began with these conditions [42], [54], [55]. According to references [56] and [57], the experimental values of the melting points of Ho, δ-Ho_2S_3, and γ-Ho_2S_3 were determined as 1734, 1952, and 1920 K, respectively. That is, at a temperature near 2000 K, the Ho metal and S will be vaporized, which could change the initial S/Ho ratio. These weight losses should be determined chemically. Thus, the temperatures of 1773, 1873, and 1973 K and heating rates of 5, 10, and 25 K/min were tested to find out the adequate compromise conditions of sintering.

2.2 Characterization by microscopic analysis

The synthesized products were identified by powder X-ray diffraction (XRD) with Cu-Kα radiation using Rint-Ultima+ (Rigaku Corp., Tokyo, Japan). The XRD was operated at a 40 kV tube voltage, a 20 mA tube current, and a 2°/min scan speed. The lattice parameters were calculated to a ±0.002 Å accuracy from the peaks of (111), (220), and (311) using Si as a standard. The phase analysis was performed by considering lines with an intensity > 3 cps.

The apparent density of the sintered compacts was measured by the Archimedes method (± 0.01 g/cm^3) using an analytical balance (AUX120, SHIMADZU Co., Japan). The actual composition of the samples was determined with the following tools:

- ICP-AES (ICPE-9820, Shimadzu, Kyoto, Japan) was used to determine the Gd and Ho content (± 0.02 at.%).
- The O contents of the initial powders and sintered samples were determined (± 0.01 at.%) with an O/N/H analyzer (EMGA-930, Horiba Ltd., Kyoto, Japan).
- The Gd (or Ho), S, and O contents were controlled through X-ray energy dispersive spectroscopy with scanning electron microscopy (EDX–SEM; JSM-6610LA, JEOL Ltd., Tokyo, Japan). The intermetallic compounds, Sm_2Fe_{17} and $SmFe_2$, made in the laboratory

were used as the calibration standard for EDX. The accuracy of the quantification procedure was within 5%.

- An optical microscope (Nikon-E400 Pol) was used to obtain microstructure images of the cross sections of the polished sintered compacts.

2.3 Apparatus for the investigation of melting point measurements

Figure 2.5 shows the thermal apparatus for measuring the melting points. These measurements were performed at the Nikolaev Institute of Inorganic Chemistry, Russia.

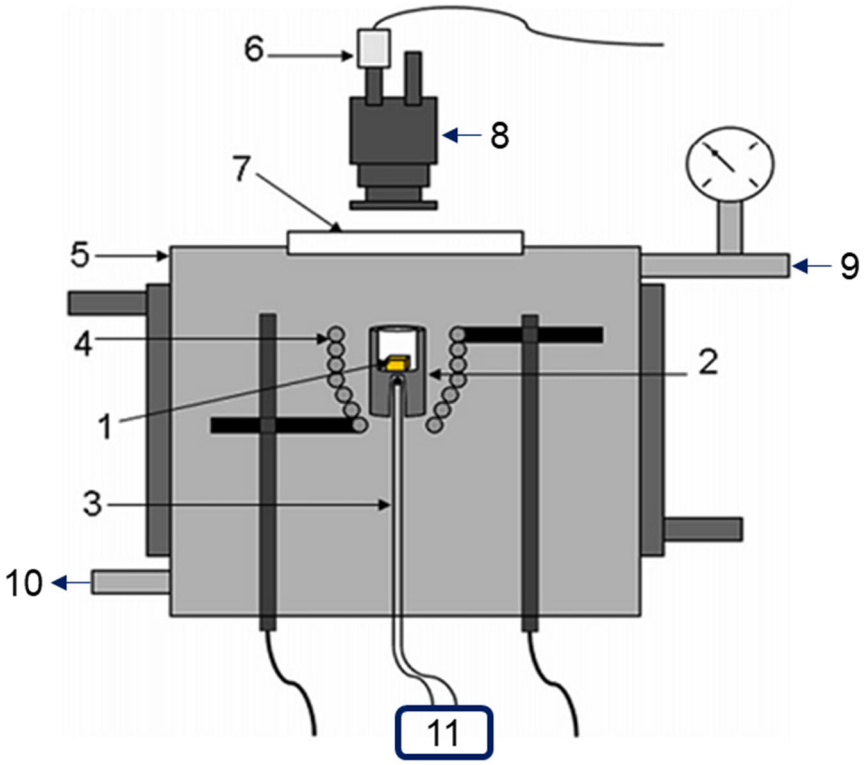

Figure 2.5 Scheme of a thermo-microscopic setup: (1) sample, (2) molybdenum crucible, (3) W/W–Re thermocouple, (4) tungsten heater, (5) sample, (6) IR photodiode, (7) optical quartz window, (8) microscope, (9, 10) vacuum and inert gas valves, and (11) computer.

The thermal stability up to the melting point was studied by using a high-temperature thermal analysis of the rapid heating and a special experimental procedure providing melting without composition variation [58]–[60]. Obtaining reliable values for the composition/melting point relationship of the non-stoichiometric GdS_x and HoS_x compacts is challenging because of their incongruent sublimation before melting. Therefore, a high-temperature thermo-microscopic apparatus operating at a wide range of heating rates and pressures of inert gases was used [21–23]. The working principle of the thermo-microscopic apparatus is based on the measurement of variations in the radiation coefficient of heating solids located in an open Mo crucible (2) by a suitable IR photodiode (mounted on a microscope (6)). To measure GdS_x and HoS_x, a 5–7 mg sample (1) was heated at a rate of 3000 K/min and at a He pressure of 7.0 atm (9). Under these conditions, a solid-vapor equilibrium was realized inside the crucible without the vapor emerging and condensing on the peephole window of the apparatus. The phase transition is recorded in the dU/dt–T coordinates, where dU/dt is the time derivative of the sample thermal radiation. The apparatus was calibrated with reference materials such as Pt (2045 K), sapphire (2333 K), and Y_2O_3 (2573 K), which allowed for the measurement of the temperature of the peaks with an accuracy of 2%. Three to five parallel measurements were conducted for each compact tested.

2.4 Electrical resistivity measurement

The electrical resistivity was measured by a standard DC four probe-method in the temperature range of 4 to 300 K using a laboratory-built physical properties measurement system for GdS and HoS with a GM refrigerator, as shown in Figure 2.6.

Figure 2.6 Electrical resistivity measurement system by laboratory-built

Figure 2.7 shows a schematic diagram of the four-probe method. The electrical resistivity, ρ, is given in equation (2.4), where V_D is the voltage drop between the two voltage probes, I is the electric current, D is a distance between the two probes, and A is cross-section of the sample. The current was applied by a current/voltage source (Model 7651, Yokogawa Corp.), and the voltage was measured with a nanovoltmeter (Model 2182A, Keithley Instruments).

$$\rho = \frac{V_D A}{DI} \tag{2.4}$$

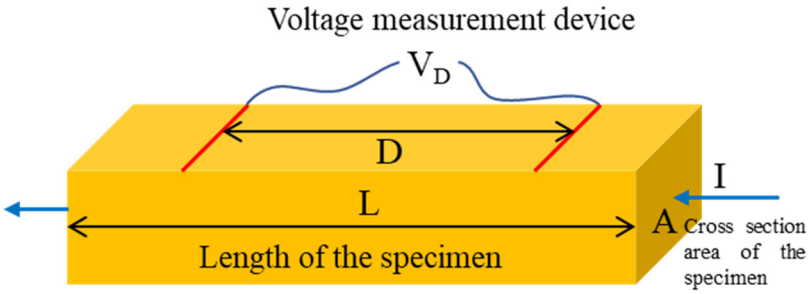

Figure 2.7 Electrical resistivity measurement by the four-probe method

Chapter 3 Results and discussion

3.1 Synthesis of RES (RE = Gd, Ho) compacts

3.1.1 GdS

a. Synthesis of GdS_x compacts

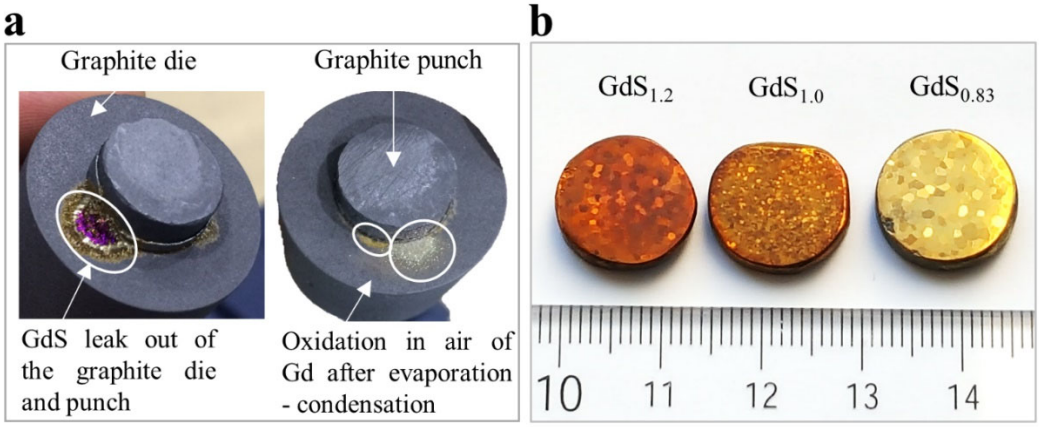

Figure 3.1. The image of the sintering die (a) and GdS compact samples (b)

Figure 3.1 shows images of (a) a sintering mold consisting of a graphite die and punch after pulsed electric current sintering and (b) the obtained sintering compacts. A gold-colored layer, resulting from the vaporization of Gd metal, was observed near the gap between the graphite die and the punch; however, this turned white when left in air (Figure 3.1(a)). This may have been a result of the evaporation and deposition of Gd owing to the decomposition of GdH_2 at high temperature [36]. In contrast, color variations (from dark copper to bright gold) of the GdS sintered compacts could be obtained by increasing the charge ratio of GdH_2, that is, 16.16 ($GdS_{1.2}$), 27.82 ($GdS_{1.0}$), and 38.15 % ($GdS_{0.83}$) (Figure 3.1(b)).

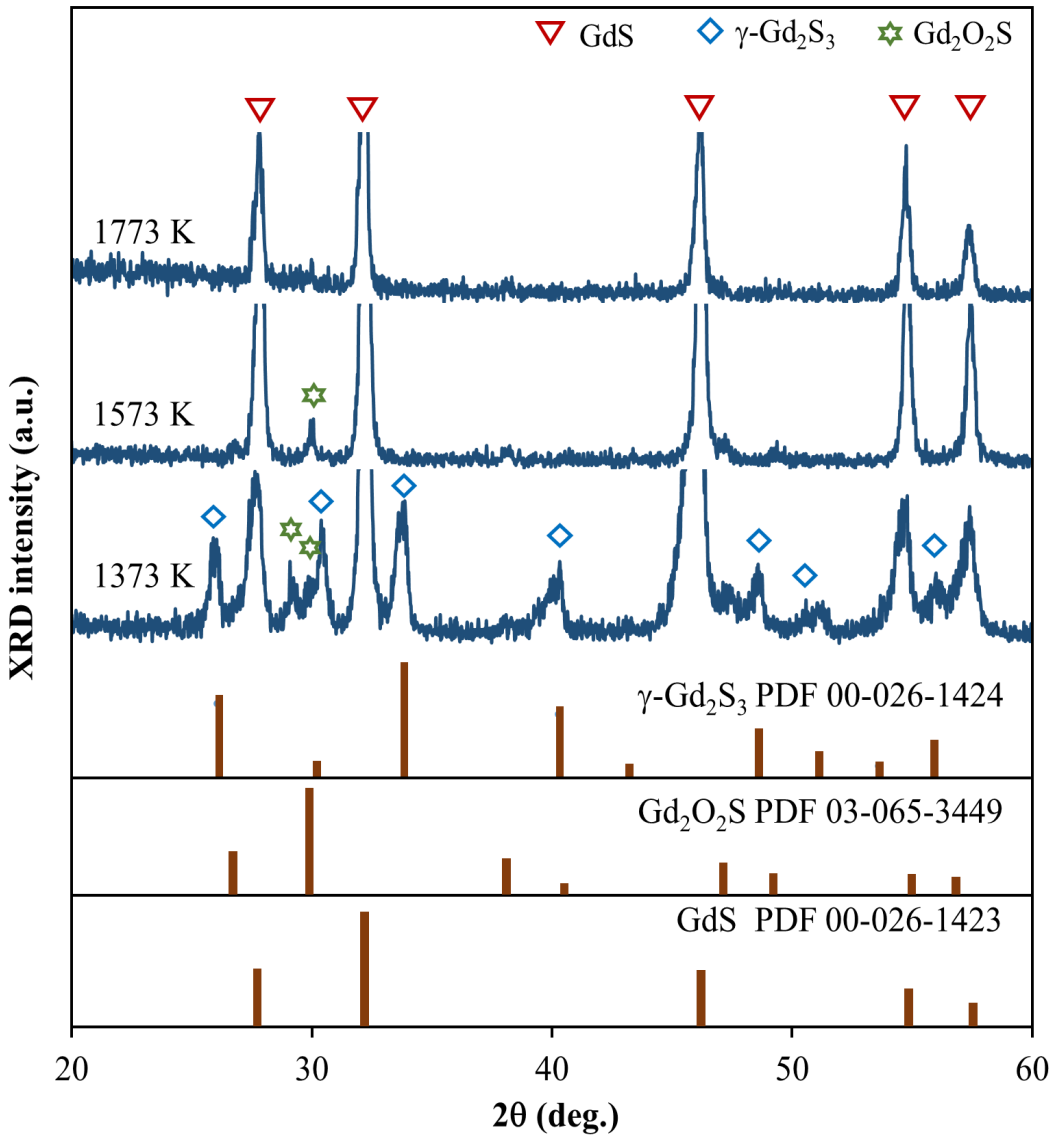

Figure 3.2. XRD results of the compacts sintered at 1373, 1573, and 1773 K

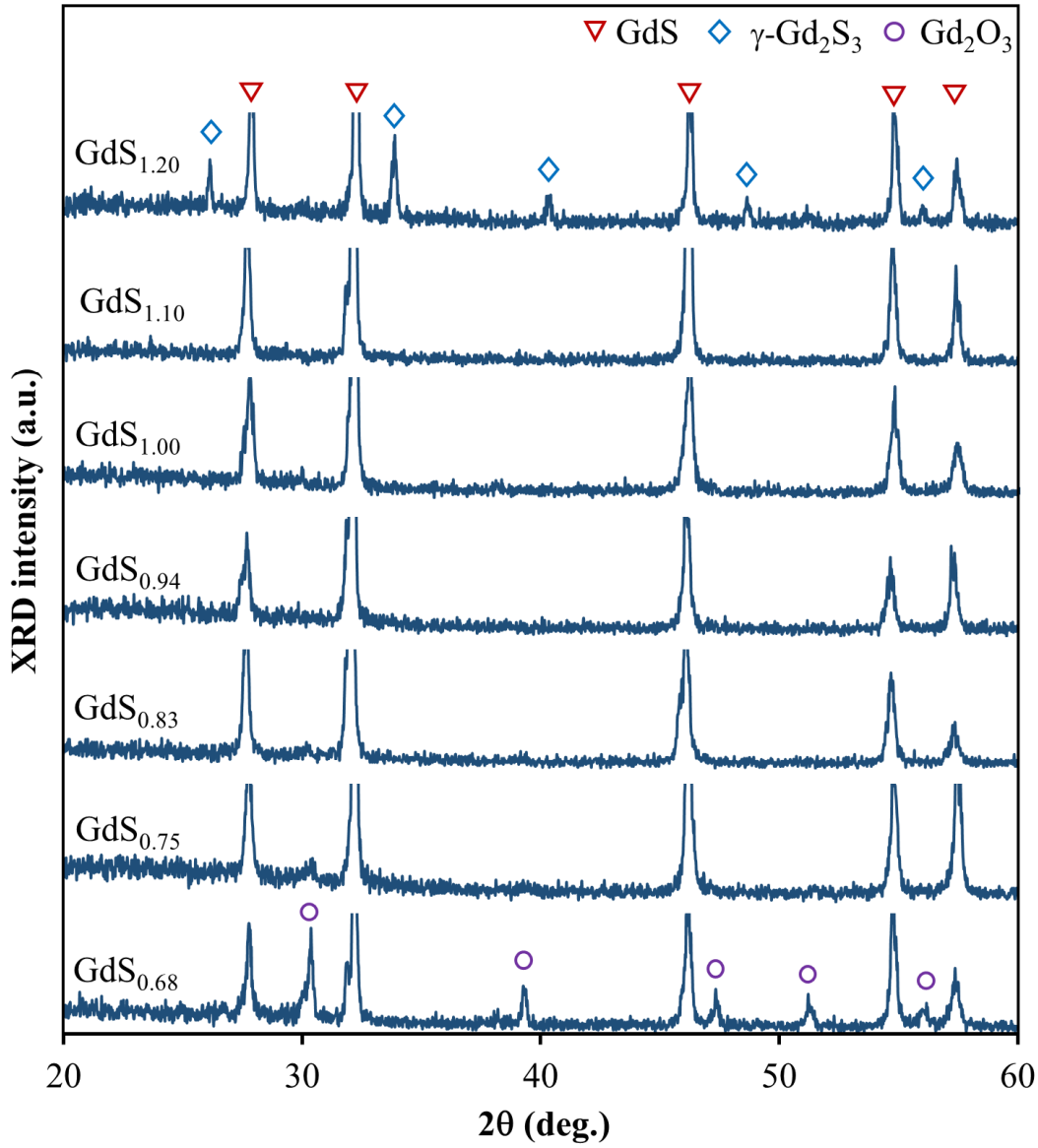

Figure 3.3. XRD results of compacts when the preparation ratios of GdH2 are adjusted at a sintering temperature of 1773 K.

Figure 3.2 shows the XRD results for the compacts sintered at 1373, 1573, and 1773 K when the preparation ratio of GdH_2 was fixed at 27.82 mass% ($GdS_{1.0}$). Figure 3.3 shows the XRD results for the compacts when the preparation ratios of GdH_2 were adjusted at a sintering temperature of 1773 K. When the sintering temperature was 1373 K, Gd_2O_2S peaks were detected, as were the peaks of γ-Gd_2S_3 transformed from α-Gd_2S_3. As the sintering temperature increased to 1573 K, the peaks of the γ-Gd_2S_3 phase disappeared and were completely replaced by GdS peaks. However, small amounts of Gd_2O_2S phases remained; these may have been formed according to Eq. (3.1)

$$2Gd_2O_{3(s)} + Gd_2S_{3(s)} = 3Gd_2O_2S_{(s)} \quad (3.1)$$

When the sintering temperature was increased to 1773 K, single-phase GdS was obtained. The formation of single-phase GdS was confirmed to not depend on the preparation ratio of GdH_2, except when this preparation ratio was extremely large or small. When the preparation ratio of GdH_2 was small, γ-Gd_2S_3 remained. Because the formation did not depend on the preparation ratio of GdH_2, the volatilization of extra Gd not contributing to the reaction was considerable. However, it was observed that the peak intensity increased and the peak became sharper when the preparation ratio of GdH_2 was increased. Moreover, it was confirmed that the crystal orientation and crystallinity of GdS increased. It was concluded from the XRD results that single-phase GdS was formed when the sintering temperature was fixed at 1773 K and when the preparation compositions were between 21.25 mass% ($GdS_{1.1}$) and 43.54 mass% ($GdS_{0.75}$).

Table 3.1. Composition of GdS_x determined from the preparation ratios and actual composition of GdS_x determined from chemical analysis

Molar ratio Gd_2S_3/GdH_2	GdH_2 (wt.%)	Preparation composition (at.%)		GdS_x[i]	Actual composition (at.%)			GdS_x[ii]
		Gd	S		Gd	S	O	
1:0.5	16.16	45.45	54.55	$GdS_{1.20}$	45.21	54.51	0.28	$GdS_{1.21}$
1:0.7	21.25	47.37	52.63	$GdS_{1.10}$	47.19	52.42	0.39	$GdS_{1.11}$
1:1	27.82	50.00	50.00	$GdS_{1.00}$	49.45	49.82	0.73	$GdS_{1.01}$
1:1.2	31.62	51.61	48.39	$GdS_{0.94}$	50.65	48.51	0.84	$GdS_{0.96}$
1:1.6	38.15	54.55	45.45	$GdS_{0.83}$	51.64	47.39	0.97	$GdS_{0.92}$
1:2	43.54	57.14	42.86	$GdS_{0.75}$	54.12	44.67	1.21	$GdS_{0.82}$
1:2.4	48.06	59.46	40.54	$GdS_{0.68}$	54.93	42.46	2.61	$GdS_{0.77}$

[i] Chemical formula calculated from the preparation composition

[ii] Chemical formula calculated from the actual composition

Table 3.1 shows the composition of GdS_x determined from (i) the preparation ratios of GdH_2 and (ii) the actual composition of GdS_x determined by chemical analysis. The sintering temperature of the compacts was 1773 K, which is consistent with the compacts identified in Figure 3.3. The x values in the GdS_x chemical formulas determined from the actual compositions were larger than those from the preparation ratios. The difference in these x values increased as the GdH_2 preparation composition was increased. These increases may have been due to the volatilization of Gd leading to a decrease in the concentration of GdS formed by the reaction shown in Eq. (3.2). The volatilization of Gd was evident in Figure 2(a). Furthermore, the O impurity content increased with an increasing GdH_2 preparation ratio. The O contents were also found to be less than the O content of α-Gd_2S_3 as a raw material, except for that at the 48.06 mass% ($GdS_{0.68}$) GdH_2 preparation ratio. These decreases in O content are thought to be due to the formation of volatile GdO by the reaction of Gd_2O_2S and Gd, as shown in Eq. (3.3). When the preparation ratio of GdH_2 was 48.06 mass% ($GdS_{0.68}$), the maximum O content reached 2.61% owing to the generation of Gd_2O_3, as shown in Figure 3.3. Bakovets *et al*. indicated that S diffusion (S_{dif}) leads to a reaction with Gd_2O_2S, yielding Gd_2S_3 and O diffusion (O_{dif}) [61]. This is related to the prediction that GdS can be formed from Gd_2O_2S at high temperatures even with a relatively high log PS_2 and log PO_2, as shown in Figure 2.4.

$$Gd_2S_{3(s)} + Gd_{(l)} = 3GdS_{(s)} \quad (3.2)$$

$$Gd_2O_2S_{(s)} + Gd_{(s)} = GdS_{(s)} + 2GdO_{(s,v)} \quad (3.3)$$

b. Density and lattice constant behavior

Table 3.2 shows the effect of the Gd content of GdS_x on the apparent density and lattice constant of the sintered compacts formed at 1773 K, which is consistent with the compacts identified in Figure 3.3 and Table 3.1. The apparent and relative densities were measured only for the single-phase sintered compacts. The apparent densities approximated the theoretically calculated values. The relative density increased as the Gd content in the preparation composition increased owing to the generation of a liquid Gd phase, which acted as a sintering additive.

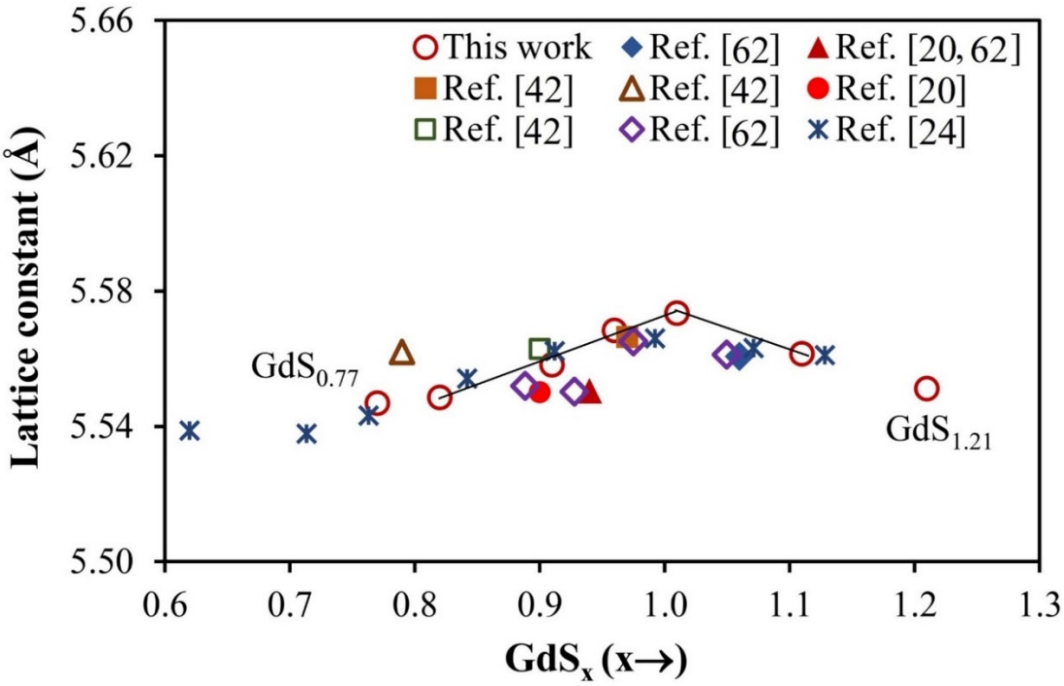

Figure 3.4. Effect of the actual composition of GdSx on lattice constant of sintered compacts.

Figure 3.4 shows the relationship between the lattice constant and the actual composition. The lattice constants reported by other authors are also provided [19], [20], [24], [42], [62]. Based on the various conditions of our experiments, the lattice

constant exhibited deviations for the same composition. However, changes in the lattice constant in response to the Gd content of GdS_x were in good agreement with conventional results [62]. A linear decrease in the lattice constant was confirmed in the actual composition range for $GdS_{0.71}$ to $GdS_{1.01}$ as the Gd content increased. A similar tendency was confirmed for the Nd, Pr, Ce, and La monosulfides, and it has been reported that the composition range that maximizes the lattice constant becomes narrower for light RE elements. However, in the actual composition range from $GdS_{1.01}$ to $GdS_{1.21}$, the lattice constant gradually decreased with a decrease in the Gd content, which also agreed with various results [62].

Table 3.2. Effect of Gd content of GdS_x on the apparent density and lattice constant of sintered compacts

Actual composition	**Lattice constant (Å)**	**Density $d_{exp.}/d_{cal.}$ (g/cm^3)**	**Relative density (%)**	**References**		
				Chemical formula	**Relative density**	**Lattice constant (Å)**
$GdS_{1.21}$	5.5511	6.43/ -	-	$Gd_{0.99}S_{1.05}$	-	5.5606 [24]
$GdS_{1.11}$	5.5615	6.56/6.88	0.953	$GdS_{0.97}$	0.9986 [62]	5.5663 [42], 5.5635 [20]
$GdS_{1.01}$	5.5735	6.99/7.26	0.962	$GdS_{0.94}$	-	5.5505 [24], [20]
$GdS_{0.96}$	5.5684	7.16/7.23	0.990	$GdS_{0.90}$	-	5.5629 [42], 5.5501 [19]
$GdS_{0.92}$	5.5581	7.20/7.22	0.997	$GdS_{0.89}$	-	5.5516 [20]
$GdS_{0.82}$	5.5485	7.25/7.10	1.021	$GdS_{0.87}$	0.9984 [62]	-
$GdS_{0.77}$	5.5468	7.28/ -	-	$GdS_{0.79}$	-	5.5619 [42]

c. Microstructural observations

The determination and distribution of the impure phases was conducted by using the EDX technique on the polished compacts using an optical microscope. Point EDX analysis was applied for the Gd, S, and O elements in different selected areas, and the chemically homogeneous areas that were found were interpreted in terms of phases. Some areas were considerably smaller than the excitation volume and could not be fully quantified by EDX, and the Gd/S and Gd/O ratios near the edge of the GdS grains could not be measured in terms of their true values because they presented an enrichment in Gd or S. The numbers in Figure 3.5, Figure *3.6*, and Figure *3.7* indicate the positions of the EDX analysis points, and the corresponding composition analysis results are shown in Table 3.3.

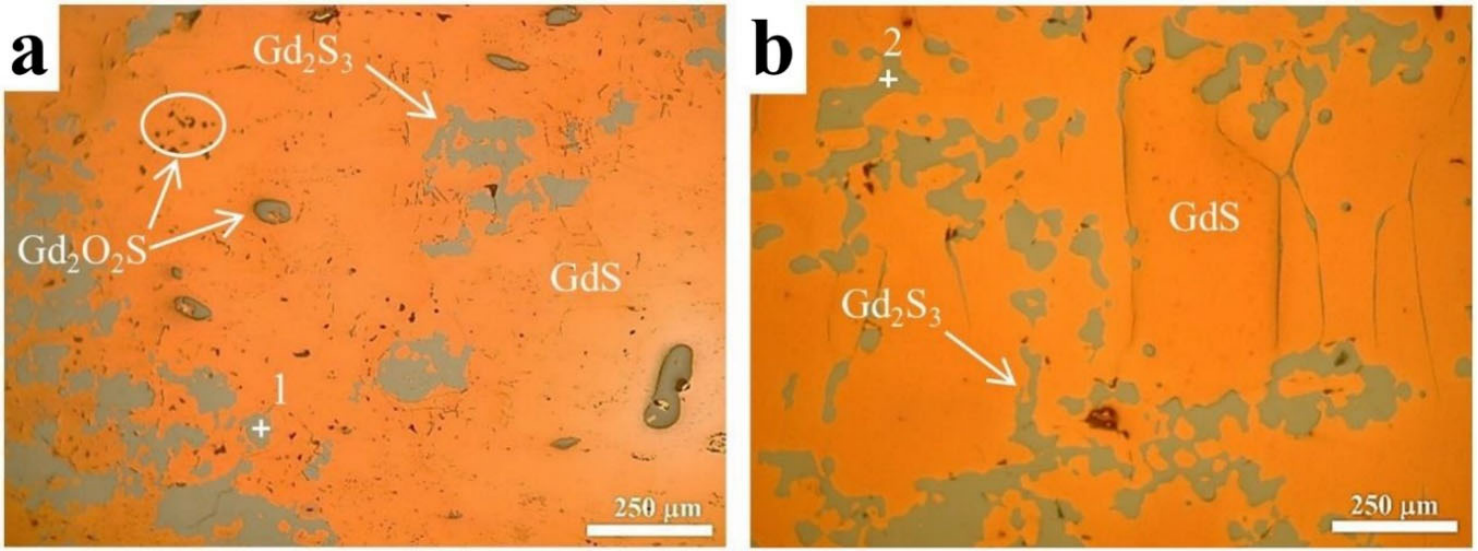

Figure 3.5.Optical microstructures of cross-sections of sintered compacts formed at (a) 1573 and (b) 1773 K when the actual composition was $GdS_{1.21}$

Figure 3.5 shows the optical cross-sectional microstructures of the sintered compacts formed at (a) 1573 and (b) 1773 K for an actual composition of $GdS_{1.21}$. The XRD results of the sintered compact with a preparation composition of $GdS_{1.0}$ (actual composition of $GdS_{1.01}$) shown in Figure 3.2 demonstrates that unreacted Gd_2S_3 remained at a sintering temperature of 1373 K. As shown in Figure 3.5, Gd_2O_2S was not confirmed at a sintering temperature of 1773 K. In contrast, when the sintering temperature was 1573 K, fine Gd_2O_2S and elliptically grown Gd_2O_2S were confirmed. Further, it was confirmed that Gd_2S_3, which was not detected by XRD in the preparation composition of $GdS_{1.0}$ (actual composition of $GdS_{1.01}$), remained at both sintering temperatures when the actual composition was 1.21. The compositions of Gd_2S_3 as precipitates were determined as $GdS_{1.55}$ for No. 1 and $GdS_{1.47}$ for No. 2 which is located near the edge of the GdS grains. The results were consistent with the understanding that the stable Gd_2S_3 precipitates are found out of the homogeneous range of the GdS phase.

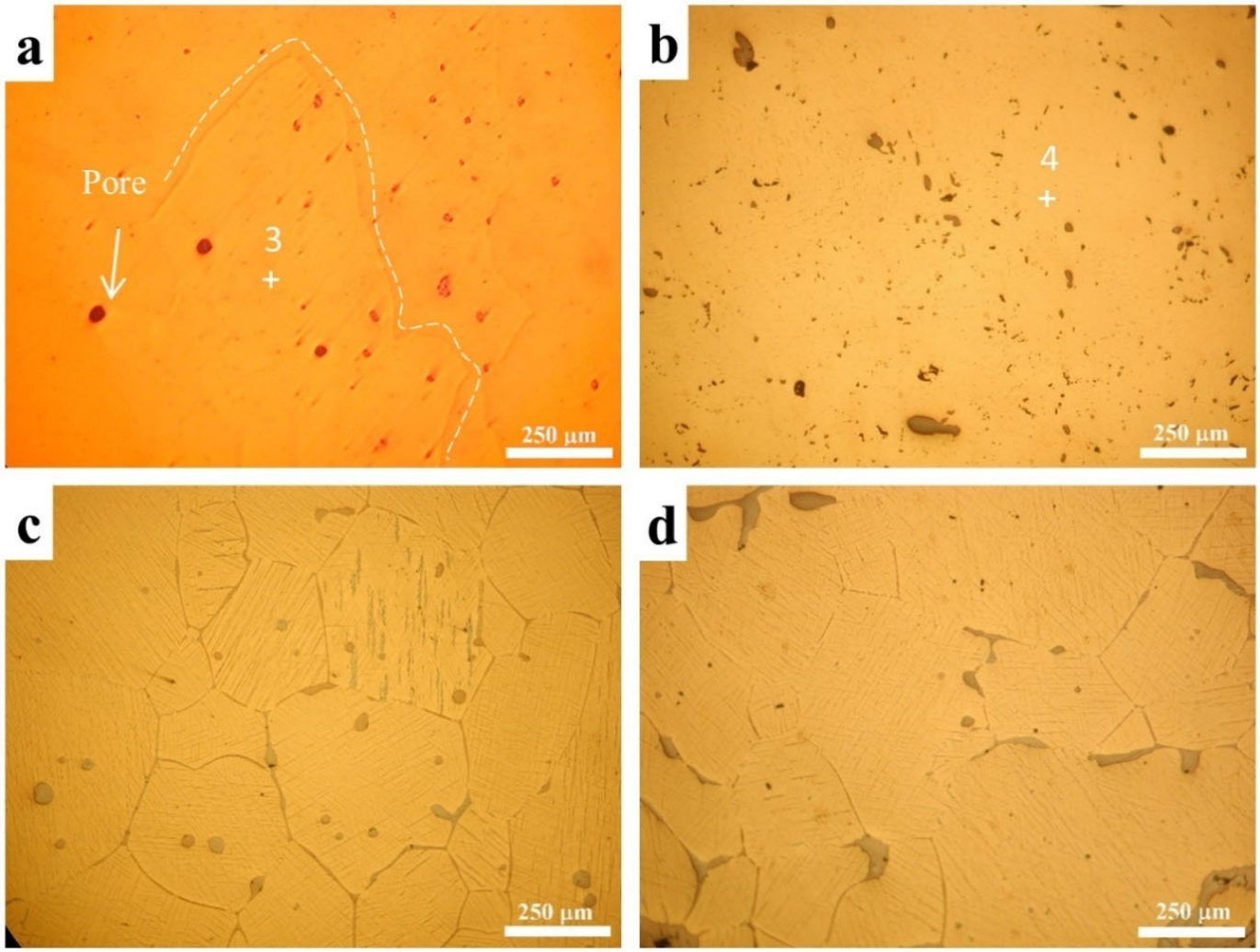

Figure 3.6.Optical microstructures of cross-sections of the sintered compact formed at 1773 K when the actual compositions were (a) $GdS_{1.01}$, (b) $GdS_{0.96}$, (c) $GdS_{0.92}$, and (d) $GdS_{0.82}$

Figure 3.6 shows the optical cross-sectional microstructures of the sintered compact formed at 1773 K when the actual compositions were (a) $GdS_{1.01}$, (b) $GdS_{0.96}$, (c) $GdS_{0.92}$, and (d) $GdS_{0.82}$. The XRD results in Figure 3.3 indicate that single-phase GdS was formed with these compositions. After polishing, a metallic colored surface exhibiting metallic bonding was obtained. Similar to the XRD result, the γ-Gd2S3 phase was not found because it was completely replaced by the GdS phase in all samples. The composition was determined as $GdS_{0.94}$ for No. 3 and $GdS_{0.92}$ for No. 4 (Table 3.3). However, precipitates were formed along the grain boundaries and spherical precipitates were formed within the grains in the cases of $GdS_{0.92}$ in Figure 3.6(c) and $GdS_{0.82}$ in Figure 3.6(d). The mean grain sizes were 302 μm and 370 μm for $GdS_{0.92}$ and $GdS_{0.82}$, respectively, and the mean grain size increased with an increasing Gd content.

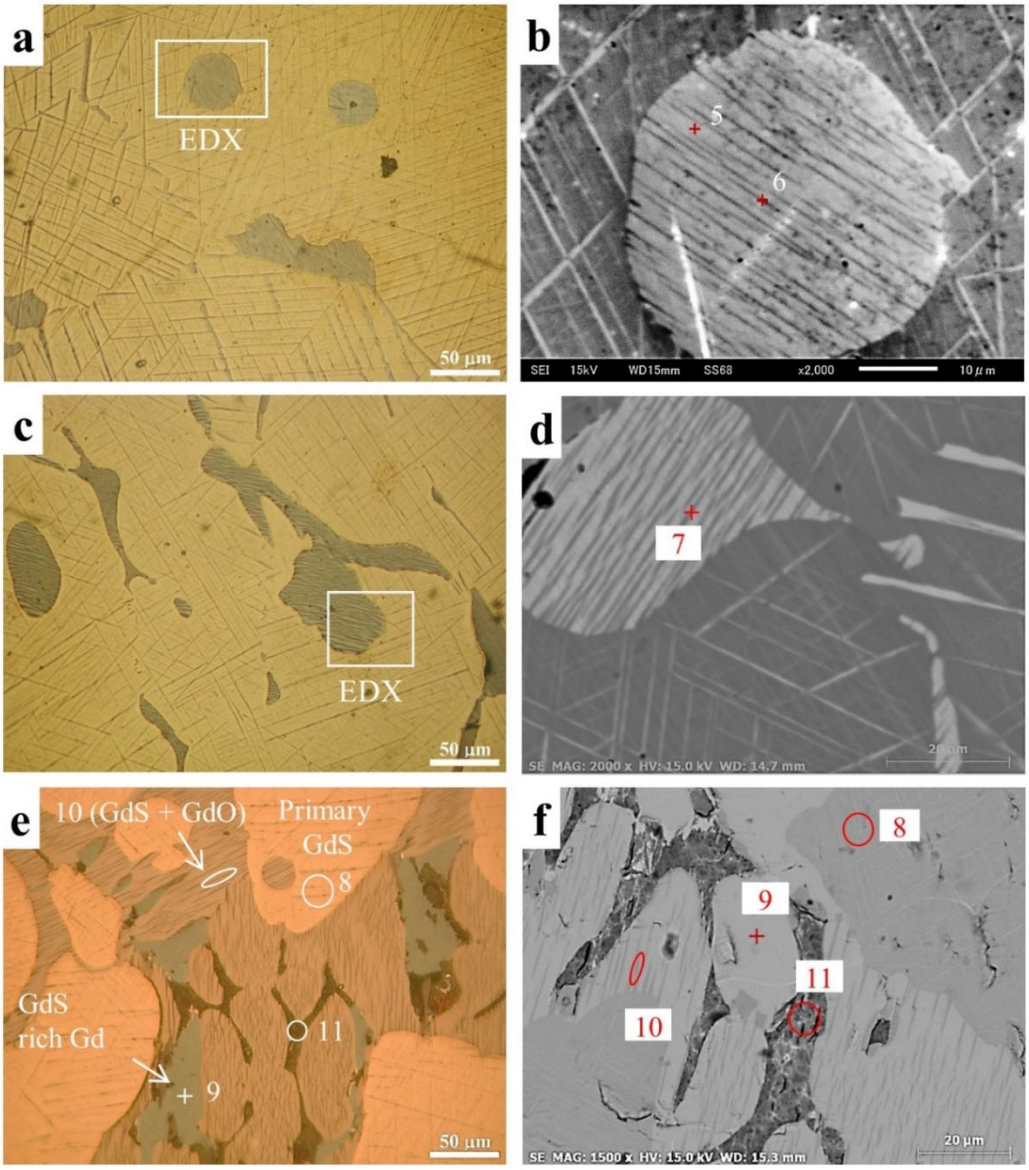

Figure 3.7. Optical microstructures and SEM microstructures of the cross-section of the sintered compact formed at 1773 K when the actual compositions were (a, b) $GdS_{0.92}$, (c, d) $GdS_{0.82}$, (e, f) $GdS_{0.77}$

Figure 3.7 shows the optical and SEM cross-sectional microstructures of the sintered compacts formed at 1773 K when the actual compositions were (a, b) $GdS_{0.92}$, (c, d) $GdS_{0.82}$, and (e, f) $GdS_{0.77}$. The XRD results in Figure 3.3 confirm that single-phase GdS was obtained (except at $GdS_{0.77}$, for which the Gd content was extremely high).

Additionally, based on point No. 5 of the $GdS_{0.92}$ EDX analysis, the spherical precipitates observed within the grains (Figure 3.6(c)) were found to be Gd with a large amount of dissolved S. They presented as a spherical shape because they were grown from a liquid phase. Furthermore, O enrichment was detected at analysis point No. 6 at the center of the spherical precipitates. The same compositions were confirmed at points No. 7 of $GdS_{0.82}$ and No. 10 of $GdS_{0.77}$. For each of these points, a composition region existed near the center of the Gd precipitate in which a large amount of S was dissolved. Bases on this composition, the precipitates may be a mixture of GdO and Gd in which a large amount of S is dissolved. There is a possibility that gaseous GdO, generated according to Eq. (3.3), condensed after remaining in the sintered compact, with liquid Gd gathering around the condensed form.

The fine particles were likely covered by a GdO layer to a certain degree if one of them began from the fixed O amount, which approximately ranged from 4% to 14%. The layer was possibly linked coherently with the metallic surface [63]. The GdO/Gd precipitates were unable to rapidly interact with Gd_2S_3 grains; thus, creating gradient zones that were enriched with different contents of S dissolved around them.

EDX analysis was performed for points No. 8 to No. 11 of $GdS_{0.77}$. When the actual composition was $GdS_{0.77}$, the maximum O content reached 2.61% owing to the generation of Gd_2O_3, as shown in Figure 3.3. Gd precipitates, in which a large amount of S was dissolved, together with precipitates around Gd_2O_3 which were enriched with O, were observed with a surrounding matrix of GdS. Being surrounded by the matrix, the particles oxidized only to GdO, whereas the metallic particles located in the free intergranular spaces of the matrix could be oxidized to Gd_2O_3 particles, which were found in the extended area of No. 11 for the $GdO_{1.51}$ composition. This can best be explained by an O grain-boundary diffusion mechanism during the sintering process.

Therefore, it is clear that when GdH_2 was added, the unreacted excess remained in the sintered compact as Gd_2O_3, Gd in which S is dissolved, and O-enriched Gd in which S is dissolved. When the amount of GdH_2 added was gradually decreased, Gd_2O_3 disappeared, and Gd in which S was dissolved and O-enriched Gd in which S was dissolved were present as precipitates in the grains and at the grain boundaries. Furthermore, as the amount of added GdH_2 was decreased to $GdS_{0.96}$, the precipitates in the GdS matrix became smaller. When the amount of GdH_2 added was less than the stoichiometric composition, the presence of unreacted Gd_2S_3 was confirmed.

Therefore, as a single-phase, according to XRD, $GdS_{0.92}$ and $GdS_{0.82}$ compacts became a heterophase through the presence of GdO/Gd and Gd_2O_3 particles, which could decrease the free carrier concentration of the compacts. Sesquioxide was detected, even with XRD, in $GdS_{0.77}$ in which the Gd content was extremely high and the maximum O content reached 2.61%. Therefore, it is interesting to consider the physical property changes of the compacts that have this microscopic phase inhomogeneity.

Table 3.3. Results of EDX point analysis at the positions shown in Figure 3.5, Figure 3.6, and Figure 3.7

EDX analysis point	**Composition at EDX analysis point (at.%)**				**Phases determined**
	S	**Gd**	**O**	**S/Gd**	
No. 1	58.5	37.5	4.0	1.55	γ-Gd_2S_3
No. 2	57.6	39.0	3.5	1.47	γ-Gd_2S_3
No. 3	46.3	49.5	4.2	0.94	$GdS_{0.94}$
No. 4	45.8	49.8	4.4	0.92	$GdS_{0.92}$
No. 5	30.9	64.5	4.6	0.48	$GdS_{0.48}$
No. 6	27.7	58.4	13.9	-	(GdS + GdO)
No. 7	25.9	53.5	20.6	-	(GdS + GdO)
No. 8	46.8	50.8	2.4	1.24	$GdS_{0.92}$
No. 9	35.9	60.7	3.4	0.59	$GdS_{0.59}$
No. 10	29.0	56.7	14.2	-	(GdS + GdO)
No. 11	1.95	38.98	59.07	1.51 (O/Gd)	$GdO_{1.51}$

3.1.2 HoS

a. Synthesis of HoS_x compacts

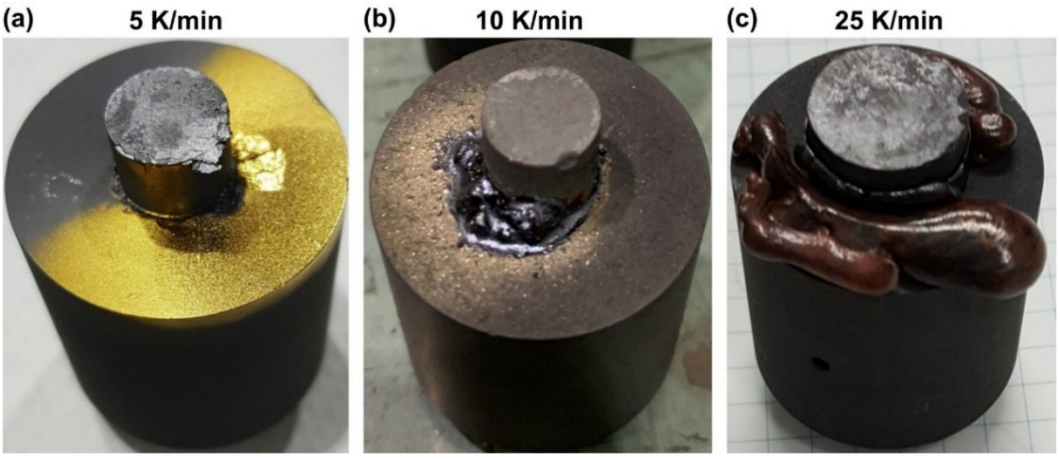

Figure 3.8 Images of the graphite punch and die after sintering at 1973 K with the heating rates of (a) 5, (b) 10, and (c) 25 K/min

Figure 3.8 shows a graphite punch and die containing the compact with an initial S/Ho ratio of 1, after sintering at 1973 K with the heating rates of 5, 10, and 25 K/min. The sintered compacts had melted and leaked out of the die at the 10 and 25 K/min heating rates. However, only a gas phase had condensed on the die lid at the 5 K/min heating rate. The golden color and the metallic luster of the condensate allowed for their identification as the HoO was being deposited [42], [55], [64]. It is presumed that in fast heating (10 and 25 K/min), the liquid Ho_2S_3 reacts with the residual O before HoS is formed, resulting in the formation of Ho_2O_2S, which has a relatively low melting point and leaked out. Slow heating (5 K/min) was favorable to both processes, namely, the Ho_2S_3 and Ho interacted with crystallization from the solid HoS melt and the vapor of the HoO in a solid state. Because this heating rate was best suited to the synthesis of pure (O-free) HoS, it was further used in the experiment.

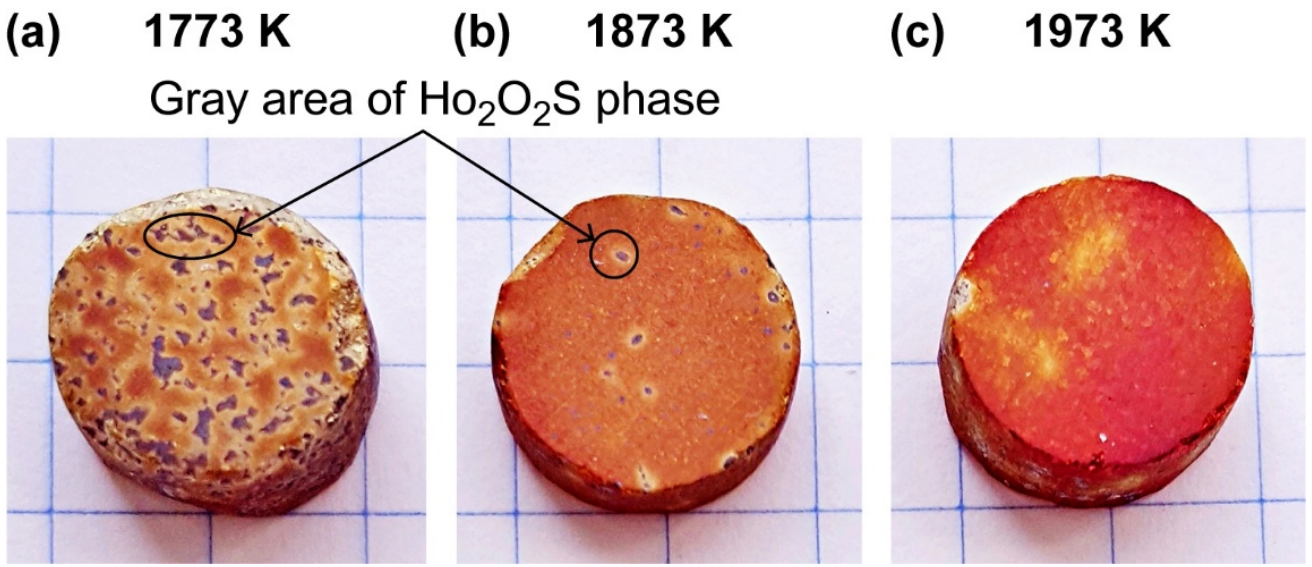

Figure 3.9 Images of the sintered compacts at sintering temperatures of (a) 1773, (b) 1873 and (c) 1973 K when the preparation ratio of the raw materials is $HoS_{1.0}$

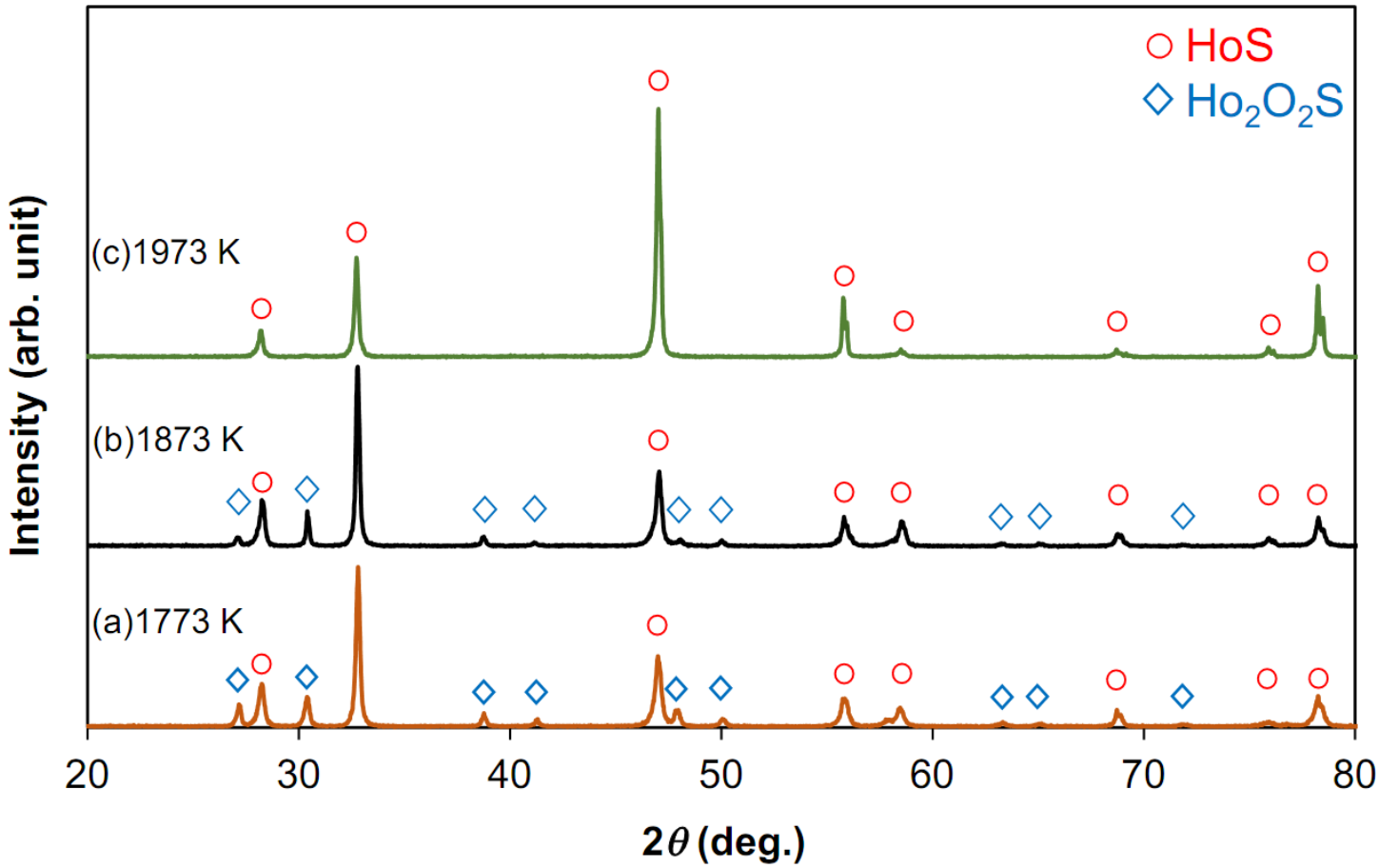

Figure 3.10 XRD patterns of the sintered compact surface in Figure 3.9

Figure 3.9 shows the surface of the polished compacts when the preparation ratio of the Ho metal was fixed at 27.82% of the mass ($HoS_{1.00}$) and sintered at 1773 K (a), 1873 K (b), and 1973 K (c). Gray-colored impurity phases were found in the compact sintered at 1773 K. The impurity phase area decreased with a higher sintering temperature. The gray color of this impurity indicated that it was the Ho_2O_2S phase. This visual observation was confirmed by the XRD patterns in Figure 3.10. The intensity of the Ho_2O_2S peaks was detectable for the compacts sintered at the two lower temperatures. These peaks disappeared at the 1973 K sintering temperature. The Ho_2O_2S disappearance was caused by the reaction between S and Ho_2O_2S, which contributed to the Ho_2S_3 production through a reaction similar to that in the GdS synthesis [53]. The occurrence of S in such conditions was dictated by the dissociative mechanism of the solid HoS phase according to Ref. [20]. In a previous study, we established a Gd–S–O diagram close to 2000 K [53], which was applied as a basis to demonstrate that the HoS phase in our experiment might also be formed from Ho_2O_2S and S because the sintering temperature at 1973 K was appropriate for ensuring the required values of log PS_2 and log PO_2.

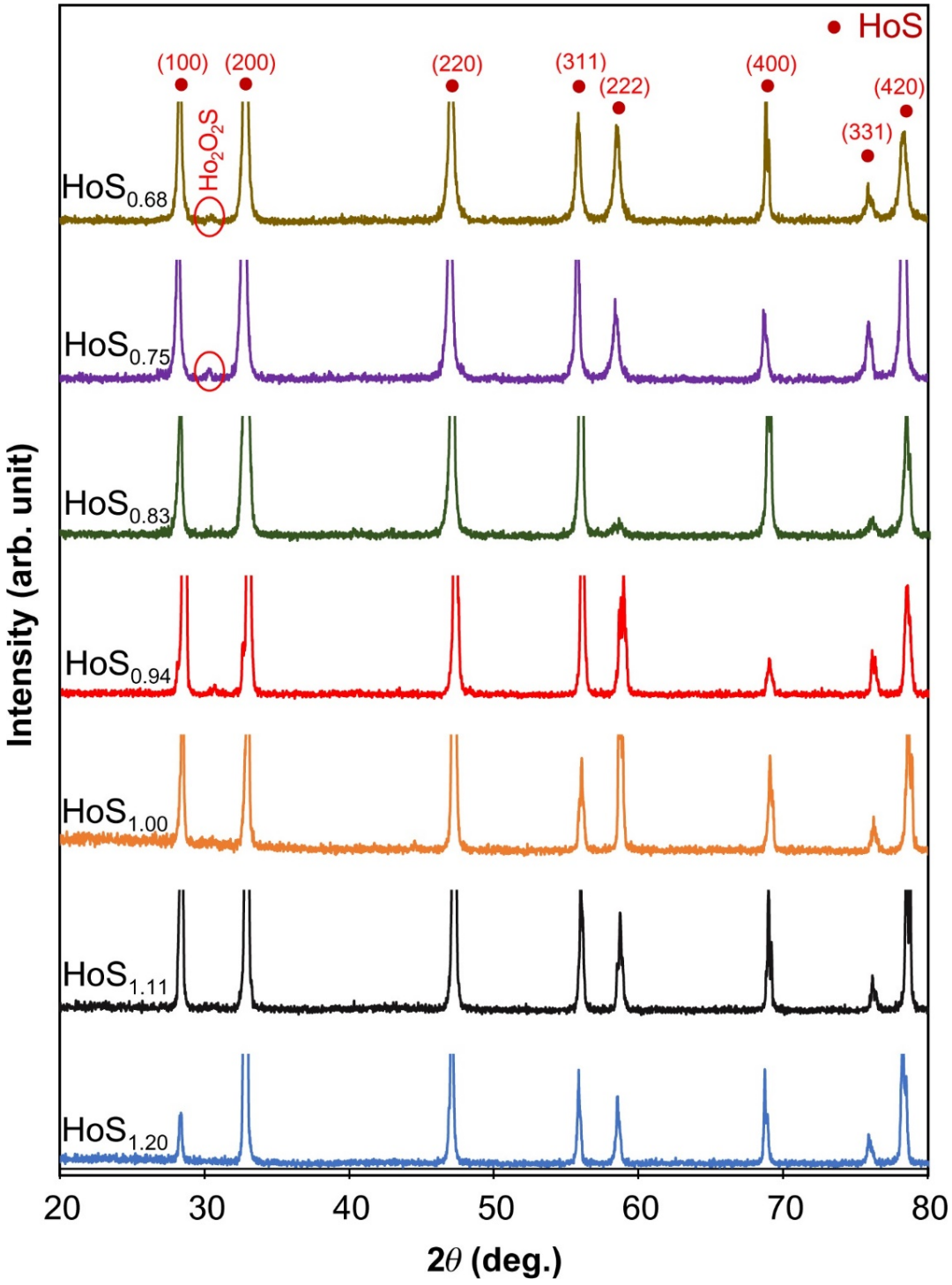

Figure 3.11 Powder XRD patterns of the HoS_x compacts sintered at 1973 K with various preparation ratios (Table 3.4)

Figure 3.11 shows the powder XRD patterns of the HoS_x compacts sintered at 1973 K with various preparation ratios of raw materials (Table 3.4). A small amount of Ho_2O_2S was detected when the preparation ratio Ho_2S_3/Ho was equal to 1: 2.0 ($HoS_{0.75}$) or 1: 2.4 ($HoS_{0.68}$). By contrast, no impurity phase was detected in the other samples, indicating that the obtained sintered compacts were a single phase. The Ho_2O_2S phase formation was obtained with the Ho metal excess. The Ho_2O_2S existence depended on the amount of Ho metal covered by the oxide film Ho_2O_3, even if the Ho_2O_3 phase remained as in our previous study [53].

Figure 3.12 depicts the color change of the compact surface (a) before and (b) after air exposure for 14 d, with the preparation ratio of the Ho metal fixed at 21.25 mass% ($HoS_{1.10}$) and the sintering temperature fixed at 1973 K. The sintered compact surface before air exposure exhibited a gold color. It turned to bright pink after air exposure for 14 d, which was a close match to the color of Ho_2O_3 oxide.

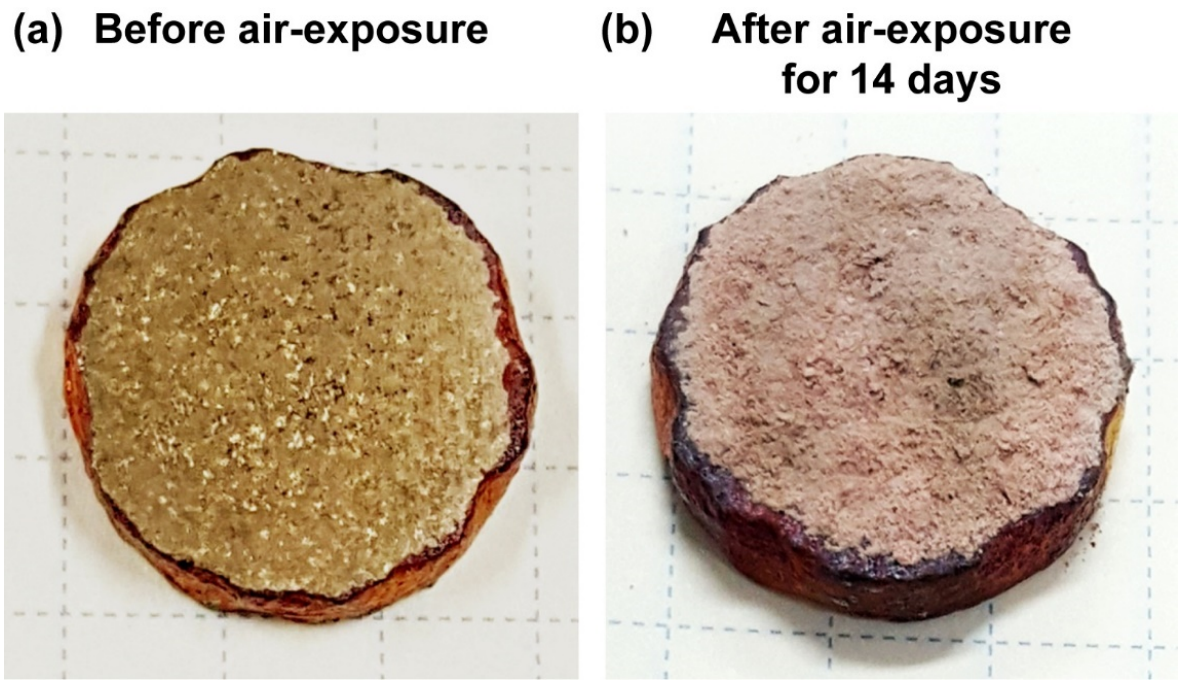

Figure 3.12 Surface change of the preparation ratio of the $HoS_{1.10}$ compact sintered at 1973 K (a) before and (b) after air exposure

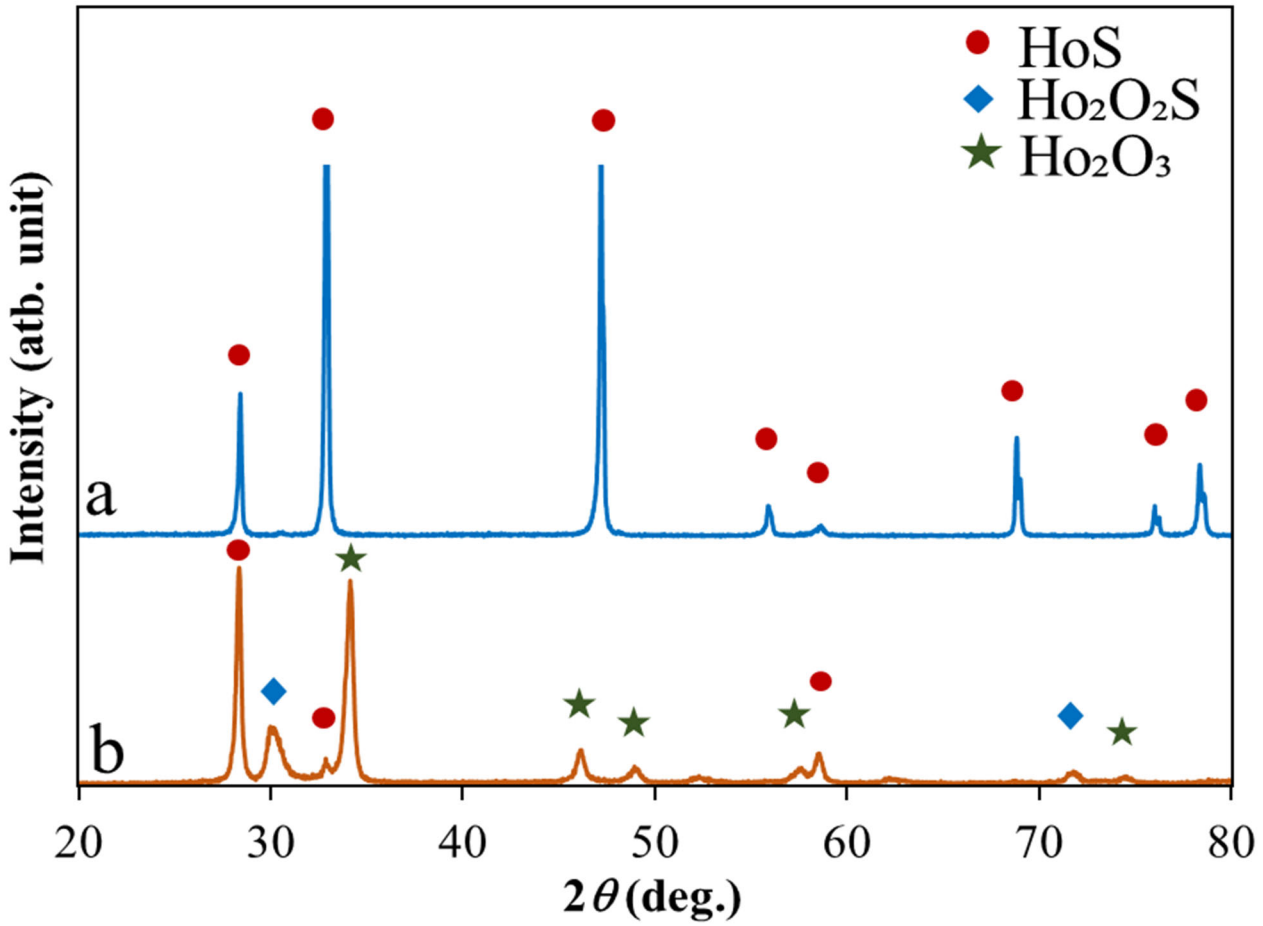

Figure 3.13 XRD patterns of the sintered compact surface in Figure 5 (a) before and (b) after air exposure for 14 days

The compact surface transformation was also analyzed by XRD and Figure 3.13 illustrates the obtained results. Ho_2O_2S and Ho_2O_3 were detected on the sintered compact surface after air exposure for 14 d, clearly demonstrating that the formation of these oxides causes a color change. In air, the initial HoO condensate was transformed into Ho_2O_3 in a process that was very slow to proceed [54]. However, oxidation did not proceed inside the sintered compacts. The surface demonstrated a yellow color after light polishing, which was typical of the compact. Therefore, after fabrication, the sintered compacts were immediately placed in a vacuum desiccator and polished again before the microscopic and electrical measurements.

Table 3.4 Preparation ratios of the raw materials and the actual ratios determined from the chemical analysis for HoS_x sintered at 1973 K

Molar ratio Ho_2S_3/Ho	**Ho (wt.%)**	**Preparation ratio (at.%)**		**HoS_x[i]**	**Actual ratio (at.%)**			**HoS_x[ii]**
		Ho	**S**		**Ho**	**S**	**O**	
1:0.5	16.16	45.45	54.55	$HoS_{1.20}$	45.43	54.1	0.46	$HoS_{1.19}$
1:0.7	21.25	47.37	52.63	$HoS_{1.10}$	47.07	52.3	0.59	$HoS_{1.11}$
1:1.0	27.82	50.00	50.00	$HoS_{1.00}$	48.47	51.1	0.42	$HoS_{1.05}$
1:1.2	31.62	51.61	48.39	$HoS_{0.94}$	49.42	50.1	0.43	$HoS_{1.01}$
1:1.6	38.15	54.55	45.45	$HoS_{0.83}$	50.00	49.7	0.31	$HoS_{0.99}$
1:2.0	43.54	57.14	42.86	$HoS_{0.75}$	50.52	47.8	1.64	$HoS_{0.94}$
1:2.4	48.06	59.46	40.54	$HoS_{0.68}$	52.55	45.1	2.31	$HoS_{0.85}$

[I] Chemical formula calculated from the preparation ratio

[ii] Chemical formula calculated from the actual ratio

Table 3.4 shows the quantitative variation of the initial S/Ho ratio caused by the losses through evaporation when the actual Ho content in the sintered compacts was determined by ICP-AES, while O was found by a specific gas analysis. The difference between the preparation and the actual values was obvious, especially for the samples with large Ho metal additions. The increase of Ho in the initial mixtures was inconsistent with the actual amount of Ho in the sintered compact. This result indicates that during sintering, Ho evaporated, and other gas-phase processes occurred. On the contrary, most of the O content increased according to the Ho addition. However, with the preparation ratio of $HoS_{1.00}$ to $HoS_{0.83}$, the O content decreased conversely in the sintered compacts. Meanwhile, the actual ratio for the analyzed $HoS_{1.05}$ to $HoS_{0.99}$ was close to the stoichiometric composition. This can be explained by HoO evaporation during the sintering process. Figure 3.8(a) clearly depicts this result. As specified in the preparation of the CeS and GdS sintered compacts [53], [55], Ce_2O_2S and Gd_2O_2S can react with metallic additions and release volatile CeO and GdO species. In this study, the same reaction, according to Eq. (3.4), was quite realistic and resulted in a lowering of the O content of the sintered compact according to the data in Table 3.4. When Ho evaporates, similar to HoO, additional Ho metal should be added to the preparation ratio to produce stoichiometric HoS. However, if there is excess Ho, the Ho_2O_3 amount will be increased according to reaction (3.5).

$$Ho_2O_2S + Ho = HoS + 2HoO \quad (3.4)$$

$$3Ho_2O_2S_{(s)} + Ho_{(s)} = 3HoS + 2Ho_2O_3 \quad (3.5)$$

b. Lattice constant and density

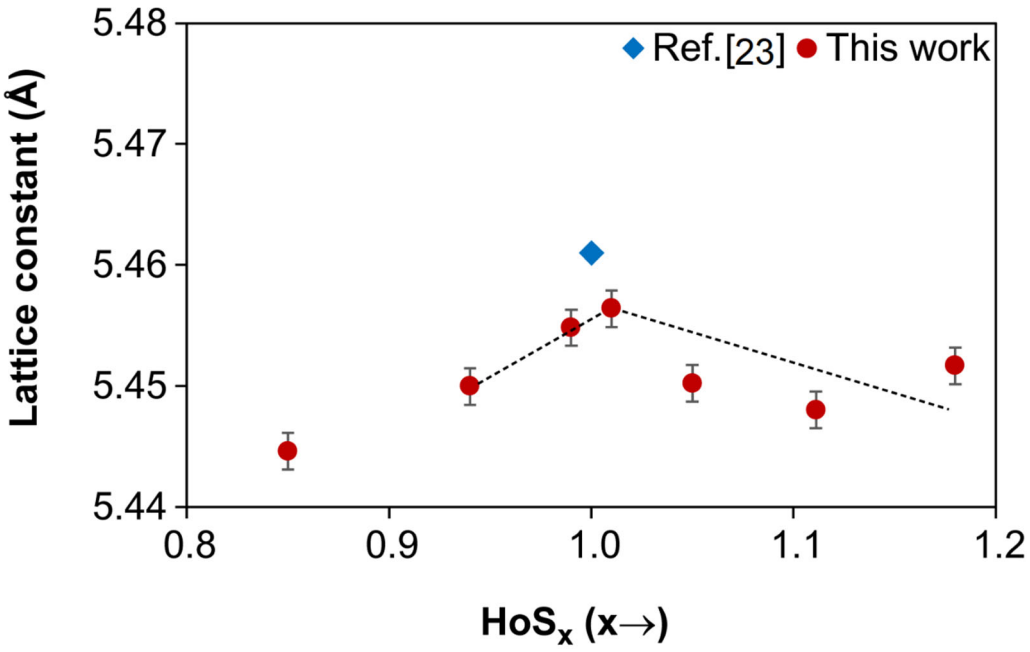

Figure 3.14 Relationship between the actual ratio and the lattice constant of HoS_x

Figure 3.14 shows the relationship between the actual ratio and the lattice constants of HoS_x sintered at 1973 K with values known from the literature [21], [23], [65], including the JCPDS 01-089-289 data. The lattice constant behavior was in a good agreement with those found in the literature. A linear increase in the lattice constant was confirmed with an increase of S in the actual ratio range from $HoS_{0.85}$ to $HoS_{1.01}$. A similar tendency was confirmed for the monosulfides of Gd, Nd, Pr, Ce, and La. Furthermore, the maximum composition range of the stoichiometric composition became narrower with light RE. Additionally, the lattice parameters in the range from $HoS_{1.05}$ to $HoS_{1.19}$ gradually decreased with the increase of S, which was also consistent with the results of Ref. [65].

Table 3.5. Apparent density of the sintered compacts formed at 1973 K

Actual	Density $d_{exp.}$	Density $d_{cal.}$	Relative density

ratio	(g/cm^3)	(g/cm^3)	(%)
$HoS_{1.19}$	6.82	6.99	0.98
$HoS_{1.11}$	7.07	7.41	0.95
$HoS_{1.05}$	7.29	7.77	0.94
$HoS_{1.01}$	7.06	8.05	0.91
$HoS_{0.99}$	7.44	8.05	0.92
$HoS_{0.94}$	7.81	8.00	0.98
$HoS_{0.85}$	7.93	7.91	1.00

Table 3.5 lists the apparent density of the sintered compacts formed at 1973 K. The nature and extension of the solid solutions for HoS were established by a correlation of the experimental density with a theoretically calculated one after transforming the actual S/Ho ratios in the real chemical formula based on the well-known model with vacancies in the metal and sulfur sublattices (Table 3.5) [21], [22], [24]. Most of the specimens were determined as a single phase by XRD, except for $HoS_{0.94}$ and $HoS_{0.85}$, of which a small amount of oxysulfide detected as a Ho_2O_2S impurity (8.07 g/cm^3) may slightly increase the experimental density. Therefore, the relative density was 98% and 100% for $HoS_{0.94}$ and $HoS_{0.85}$, respectively, while 91–96% of the values were observed for the single-phase compacts.

c. Microstructures and EDX analysis

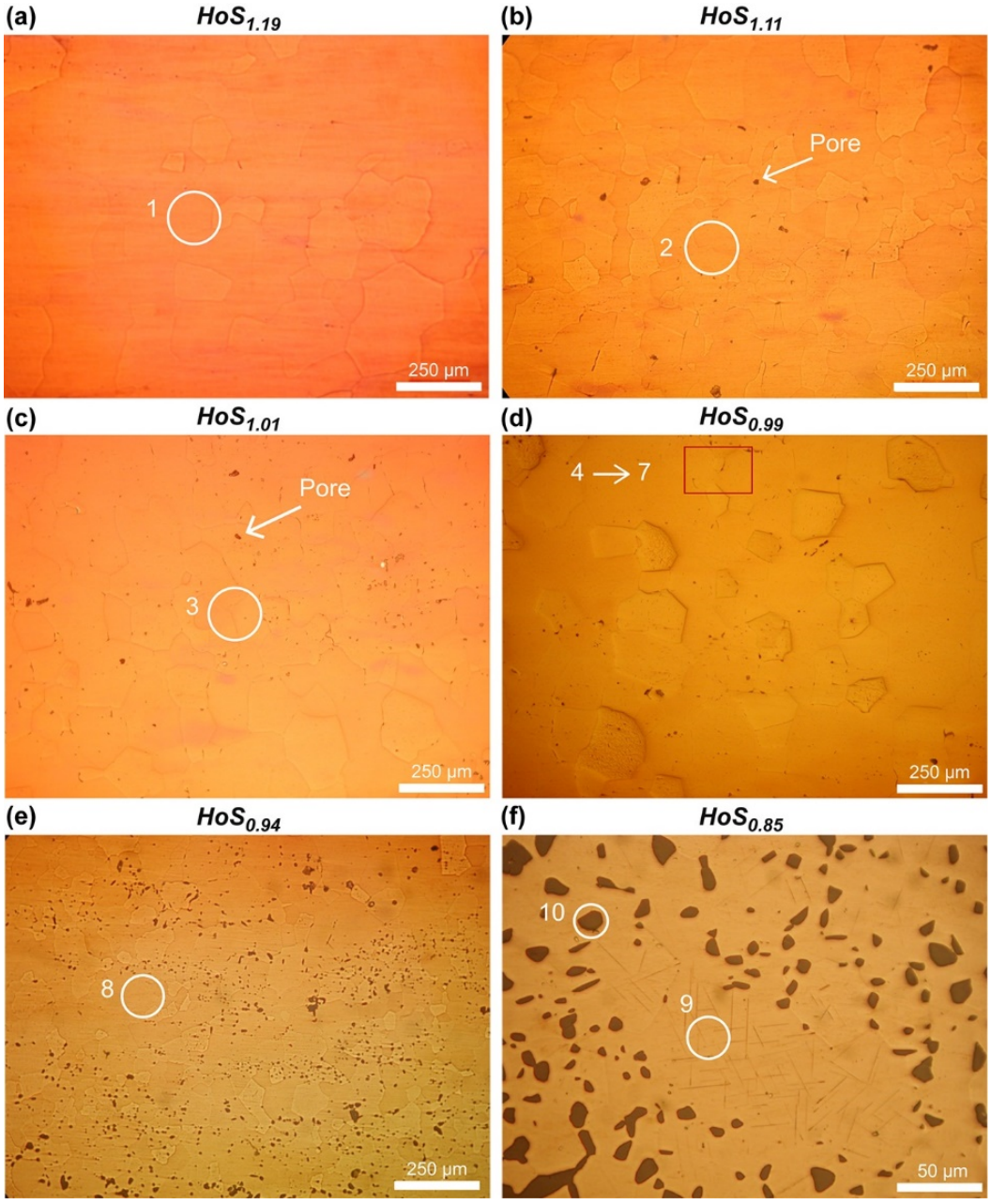

Figure 3.15. Optical microstructures of the cross-sections of the sintered compact formed at 1973 K, where the actual ratios are (a) $HoS_{1.19}$, (b) $HoS_{1.11}$, (c) $HoS_{1.01}$, (d) $HoS_{0.99}$, (e) $HoS_{0.94}$, and (f) $HoS_{0.85}$

Figure 3.15 shows the optical cross-sectional microstructures of the HoS_x sintered compact formed at 1973 K, where the actual ratios were (a) $HoS_{1.19}$, (b) $HoS_{1.11}$, (c) $HoS_{1.01}$, (d) $HoS_{0.99}$, (e) $HoS_{0.94}$, and (f) $HoS_{0.85}$. Figure 3.15(a) shows that the surface of the sintered $HoS_{1.19}$ compact was homogenous without any precipitation even on the microscopic level. For $HoS_{1.11}$, $HoS_{1.01}$, and $HoS_{0.99}$, in Figure 3.15(b–d), some nano-sized precipitates were observed at the grain boundaries, which were not present on the XRD patterns in Figure 3.11. A well-defined two-phase microstructure was observed for $HoS_{0.85}$, where large precipitates were located between matrix grains. These Ho_2O_2S impurities, whose formation became possible because of the greatest amount of initial Ho incorporated into the sample.

Having an equiaxed grain structure, the average grain size for the $HoS_{1.19}$, $HoS_{1.11}$, and $HoS_{1.01}$ compacts were determined as 184, 147, and 133 μm, respectively. The grain size decreased when the preparation ratio of the Ho metal increased. $HoS_{0.99}$ comprised a mixture of coarse grains (162 μm) and fine grains. At the same time, the microstructures demonstrated dense grain packing without an extended interface. This is an advantage of liquid-phase sintering at 1973 K, where the mutual dissolution of Ho and δ-Ho_2S_3 provides crystallization and intergrowth of the HoS grains. Numerous line defects were observed on the crystal faces, where no precipitates were found.

Table 3.6. Apparent density of the sintered compacts formed at 1973 K

Area	Chemical compositions (at.%)				Phases determined
	Ho	S	O	S/Ho	
A1	45.43	51.22	3.34	1.13	$HoS_{1.13}$
A2	46.19	50.26	3.55	1.09	$HoS_{1.09}$
A3	47.94	49.98	2.07	1.04	$HoS_{1.04}$
A4	48.81	48.78	2.40	1.00	HoS
A5	48.55	49.16	2.28	1.01	$HoS_{1.01}$
A6	49.26	48.67	2.07	1.01	$HoS_{1.01}$
A7	48.97	49.06	1.97	1.00	HoS
A8	50.48	47.80	1.71	0.95	$HoS_{0.95}$
A9	52.55	43.41	4.04	0.83	$HoS_{0.83}$
A10	45.50	21.57	32.92	-	Ho_2O_2S

To determine the correlation between the color and the actual composition of the HoS_x compacts, the SEM/EDX analysis of the polished samples was performed using an optical microscope. In the areas marked as A1-A10, all three components were determined for the presentation of the actual chemical formula of the compacts. The impurity phase inclusion was also reliably identified and presented in Table 3.6. The atomic compositions of the matrix, determined by EDX, were consistent with those determined by the ICP–AES analysis (Table 3.4). The analysis also presented precipitates which were observed in the actual ratio of $HoS_{0.85}$ to Ho_2O_2S. This result agreed with the XRD measurements in Figure 3.11.

3.2 Electrical properties

3.2.1 Electrical properties of GdS

Figure 3.17 shows the dependence of the preparation composition (actual composition) on the electrical resistivity (ρ) at room temperature of the sintered compacts formed at a 1773 K. The behavior of σ is similar to the previously reported behavior of GdS_x with $0.68 \leq x \leq 1$ [19]. It has also been reported that the electrical conductivity depends strongly on the x value owing to free carrier localization and additional electron scattering at lattice defects [19].

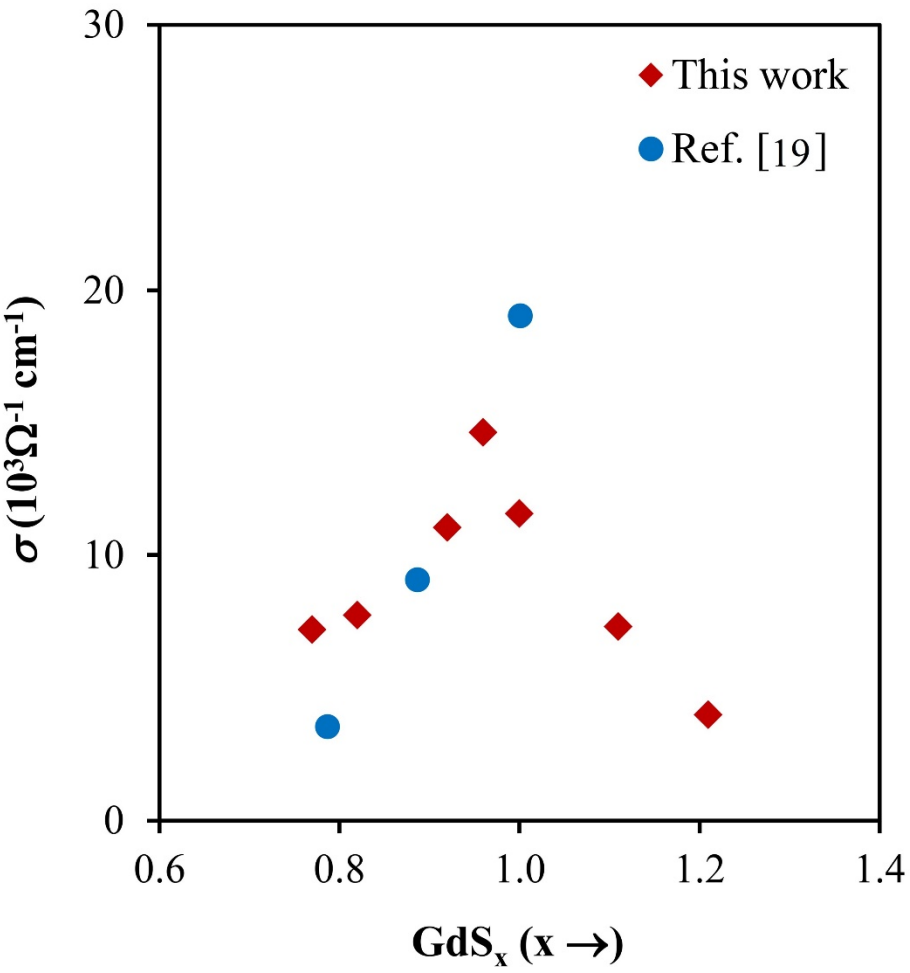

Figure 3.16. Dependence of actual composition on electrical conductivity (σ) at room temperature of sintered compacts formed at a sintering temperature of 1773 K

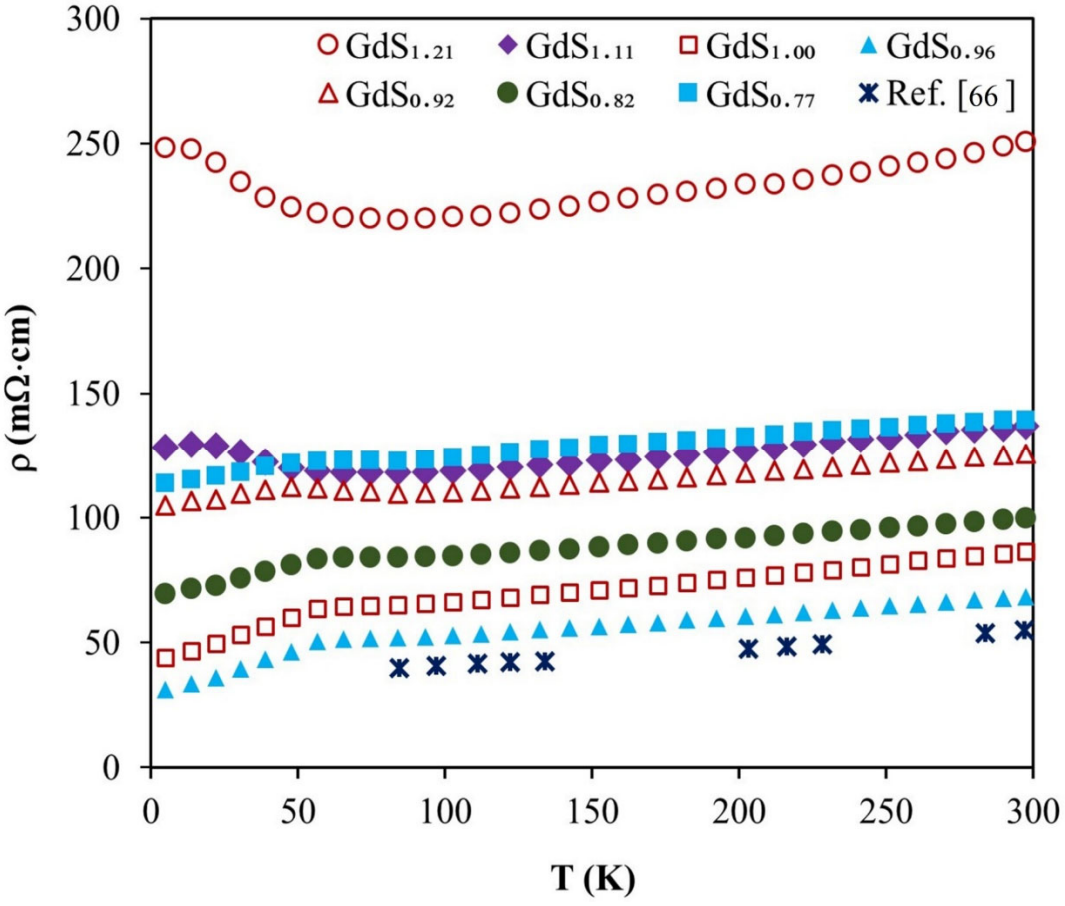

Figure 3.17. Temperature dependence of the electrical resistivity of the sintered compacts shown in Figure 3.1

Figure 3.18 shows the temperature dependence of electrical resistivity of the sintered compacts shown in Figure 3.1(b), and those reported in the literature [66]. It can be seen that the Néel temperature of GdS is approximately 56.6 K [67]. Thus, when the actual compositions were $GdS_{1.11}$ and $GdS_{1.21}$, the electrical resistivity showed a semiconductor behavior at temperatures of 56.6 K or less. In contrast, the electrical resistivity showed metallic behavior at temperatures above 56.6 K. When the actual composition was in the $GdS_{0.77}$ to $GdS_{1.01}$ range, the electrical resistance had a positive temperature coefficient and thus showed metallic behavior.

Herein, an abnormal behavior of the resistivity temperature dependencies for GdS_x with an excess of Gd was detected, which was the resistivity of $GdS_{0.77}$, $GdS_{0.82}$, and $GdS_{0.92}$ that were located closer to the $GdS_{1.11}$ compact than to $GdS_{0.96}$. The correlation between the abnormal and O-induced defects was caused by the values of 2.61, 1.21, and 0.97 at.% for $GdS_{0.77}$ $GdS_{0.82}$, and $GdS_{0.92}$ compacts, respectively, and imperfections in the microscopic phase with the low-dimensional GdO/Gd and Gd_2O_3 particles. Moreover, the $GdS_{1.01}$ and $GdS_{0.96}$ compacts were free from such defect types, demonstrating the lowest resistivity. This suggests that microscopic O-induced imperfections complicate the correct interpretation of the electric properties of the GdS_x phase purity only through XRD; therefore, microscopy is an indispensable analysis technique to study the actual RES characteristics.

3.2.2 Electrical properties of HoS

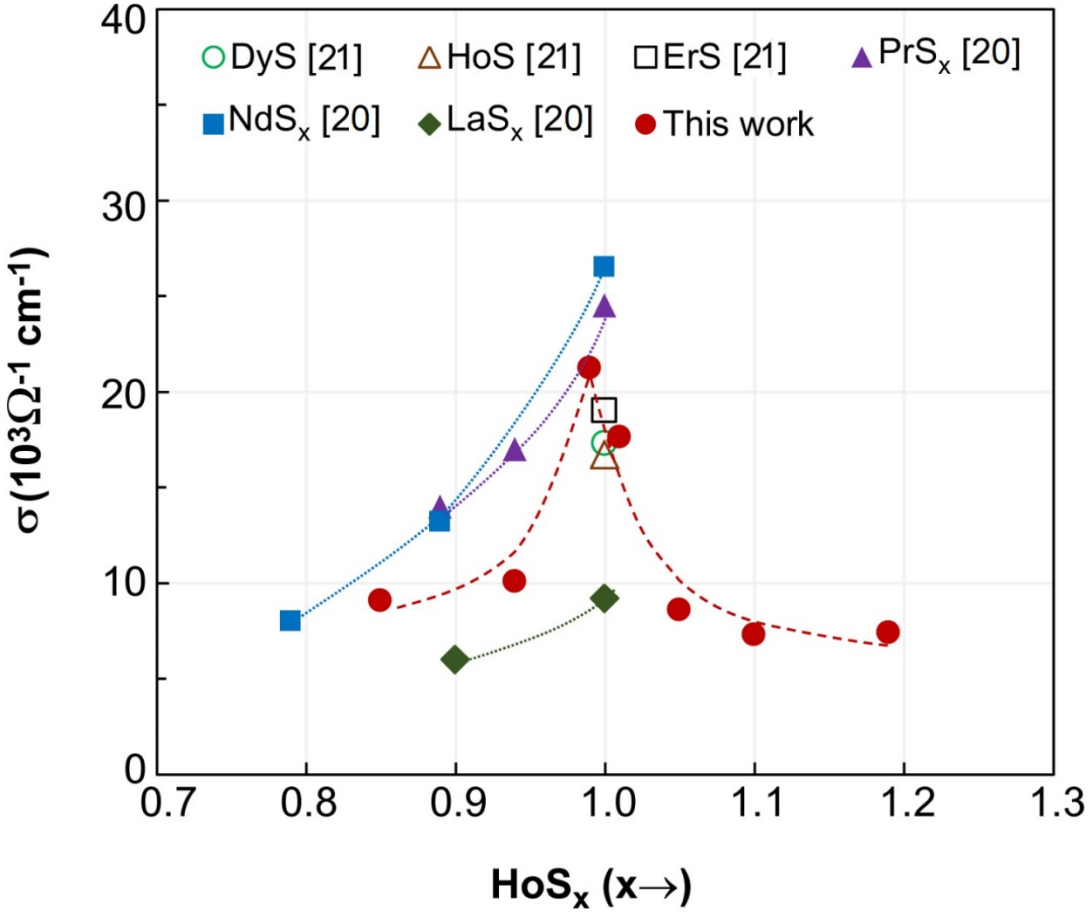

Figure 3.18 Relationships between the electrical conductivity (σ) measured at room temperature and the actual composition of the HoS_x compacts sintered at 1973 K

Figure 3.18 shows the relationships between the S content (x) of the actual ratios and the electrical conductivity (σ) of the HoS_x sintered at 1973 K and measured at room temperature. The conductivity exhibited a maximum when x was close to the stoichiometric sample, namely $HoS_{0.99}$. A similar tendency was also reported in the isostructural compounds of PrS_x, NdS_x, and LaS_x in Figure 3.18 [19]. Our maximum value for $HoS_{0.99}$ was lower than that for PrS and ErS, but higher than that obtained previously for HoS [21].

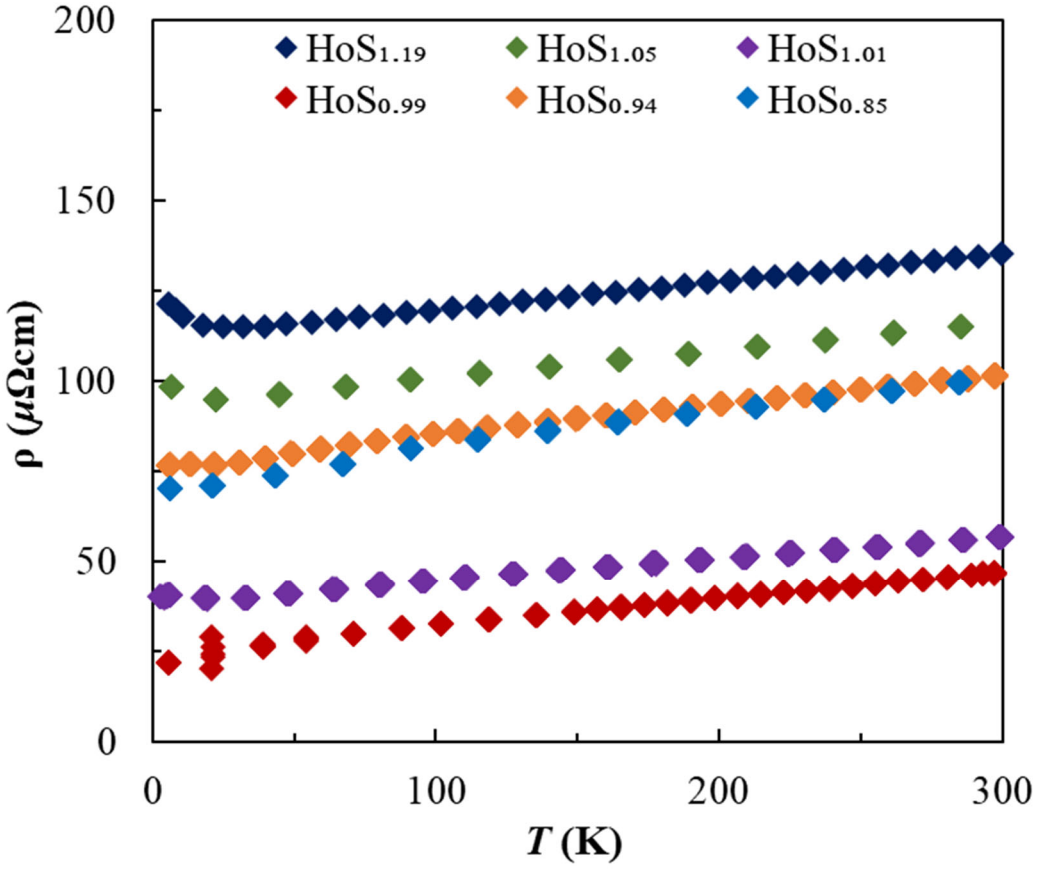

Figure 3.19 Temperature dependence of the electrical resistivity (ρ) versus the actual composition of the HoS_x compacts sintered at 1973 K

Figure 3.19 presents the temperature dependence of the electrical resistivity (ρ) of HoS_x as the actual ratio of compacts sintered at 1973 K. All HoS_x showed metallic behaviors down to 50 K. However, below 20 K, a semiconducting-like upturn was observed, except for $HoS_{0.99}$. A similar behavior was also observed in the nonstoichiometric GdS_x [53], which was explained by some lattice imperfections arising from the partial oxidization of the grains and the S defects. For $HoS_{0.99}$, whose chemical composition was the closest to stoichiometric, the upturn of ρ was not observed. Meanwhile, ρ decreased with the decreasing temperature below the Néel temperature of 21 K. Therefore, $HoS_{0.99}$ and $HoS_{1.19}$ presented the lowest and highest ρ, respectively. The difference is easily explained by focusing attention on their microstructures.

3.3 Melting point measurement

3.3.1 Melting point of GdS

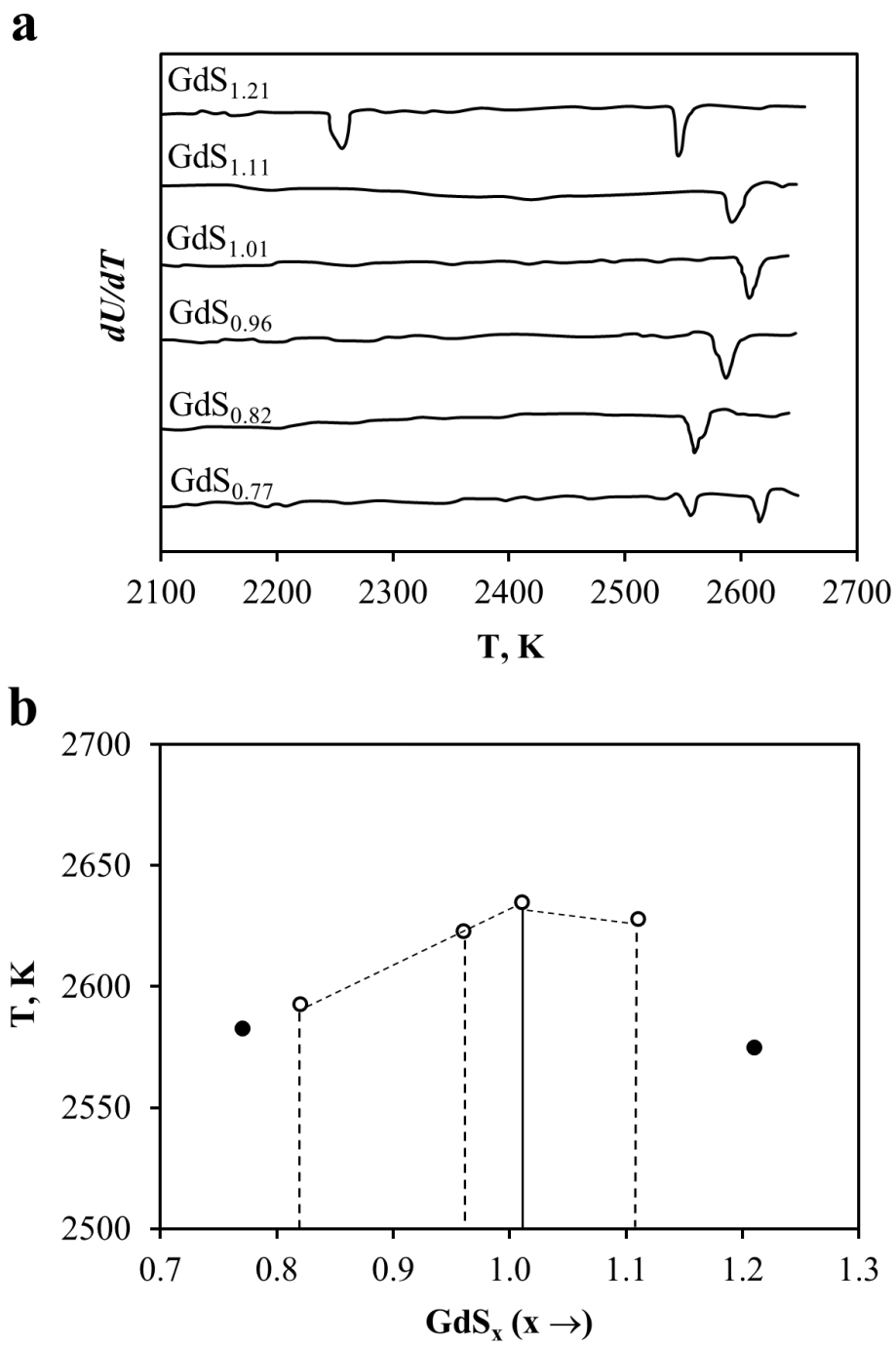

Figure 3.20. Heating curves (a) and liquidus line in the homogeneous range (b) for the compacts sintered at 1773 K

Figure 3.20 shows the high-temperature thermal analysis results for determining the melting point of GdS_x sintered at 1773 K. As shown, in this temperature range, curves with either one or two peaks were observed. It is clear that the former sintered compacts were single-phase GdS_x, whereas the latter were multiphases of GdS_x and an impurity phase. In the case of $GdS_{1.21}$, the peak at 2200 ± 40 K coincided with the melting point of Gd_2S_3, which has been reported as 2160 [40] and 2180 K [68]. For $GdS_{0.77}$, a peak at approximately 2650 K coincided with the melting point of Gd_2O_3, which has been reported as 2595 K [68]. Figure 3.20(b) shows the relationship between the actual composition and the melting point in the composition range in which formation of a single phase was also confirmed in Figure 3.20(a). The melting points of $GdS_{0.82}$, $GdS_{0.96}$, $GdS_{1.01}$, and $GdS_{1.11}$ were 2593, 2623, 2633, and 2628 K, respectively.

3.3.2 Melting point of HoS

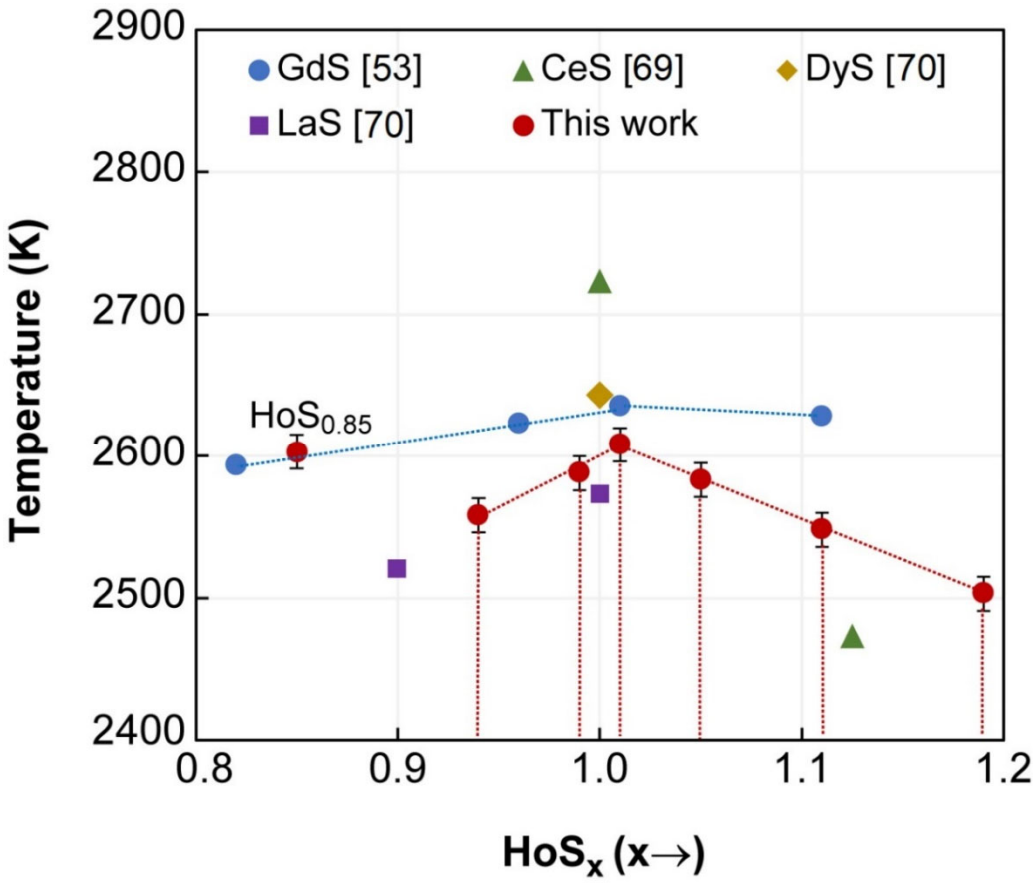

Figure 3.21 Melting points versus actual compositions of the HoS_x compacts sintered at 1973 K

Figure 3.21 depicts the melting point of HoS_x together with the data of other RES taken from Refs. [53], [69], [70]. The melting point increased as x approached the stoichiometric composition of 1.00. Within the experimental error, 30 K, the melting points of $HoS_{1.19}$, $HoS_{1.11}$, and $HoS_{1.05}$ were 2530, 2548, and 2583, respectively. Being close to stoichiometry, both compacts with $HoS_{1.01}$ and $HoS_{0.99}$ showed the same highest melting point value of 2608 ± 30 K. This similar tendency was found in the isostructural compounds of CeS [69], LaS [70], and DyS [70].

Chapter 4 Conclusions

Large and dense homogeneous non-stoichiometric GdS_x (HoS_x) was successfully synthesized by the reaction sintering of Gd_2S_3 and GdH_2 (Ho_2S_3 and Ho) using SPS.

Additionally, the effects of metal Gd (or Ho) addition within the homogeneity range of the GdS (or HoS) phase on the lattice constants, microstructure, melting point, and electrical resistivity were studied. The lattice constant and the melting temperature gradually increased when the composition was close to the stoichiometric composition. The electrical conductivity also increased when the actual composition was close to stoichiometric. In contrast, when the composition was far from stoichiometric, a semiconducting like-behavior appeared at the magnetic ordering temperature.

The developed synthesis process could be applied to synthesize other RES. Additionally, this study demonstrated two practically important innovations that have not been reported previously, namely, a methodology that describes the preparation of stoichiometric compacts enriched by RE metal with no or a minimum content of impurities, and how to systematically identify the effect of defects on the chemical and physical properties in cases where they are quite rare.

References

[1] G. Meyer and L.R. Morss, Synthesis of lanthanide and actinide compounds, 321-352, Kluwer Academic Publishers, Norwell, pp.1991, 1991.

[2] Y. Modukuru, J. Thachery, H. Tang, A. Malhotra, M. Cahay, and P. Boolchand, "Growth and characterization of rare-earth monosulfides for cold cathode applications," J. Vac. Sci. Technol. B Microelectron. Nanom. Struct., vol. 19, no. 5, pp. 1958–1961, 2001, doi: 10.1116/1.1406158.

[3] M. Cahay et al., "Review Article: Rare-earth monosulfides as durable and efficient cold cathodes," J. Vac. Sci. Technol. B, Nanotechnol. Microelectron. Mater. Process. Meas. Phenom., vol. 29, no. 6, p. 06F602, 2011, doi: 10.1116/1.3653275.

[4] D. Asai et al., "Valence fluctuations and giant isotropic negative thermal expansion in Sm1- x R xS (R = Y, La, Ce, Pr, Nd)," Appl. Phys. Lett., vol. 114, no. 14, 2019, doi: 10.1063/1.5090546.

[5] A. Sousanis, P. F. Smet, and D. Poelman, "Samarium monosulfide (SmS): Reviewing properties and applications," Materials (Basel)., vol. 10, no. 8, 2017, doi: 10.3390/ma10080953.

[6] D. X. Li et al., "Large reversible magnetocaloric effect in ferromagnetic semiconductor EuS," Solid State Commun., vol. 193, pp. 6–10, 2014, doi: 10.1016/j.ssc.2014.05.024.

[7] I. Jarrige et al., "Unified understanding of the valence transition in the rare-earth monochalcogenides under pressure," Phys. Rev. B - Condens. Matter Mater. Phys., vol. 87, no. 11, pp. 1–5, 2013, doi: 10.1103/PhysRevB.87.115107.

[8] A. Sousanis, P. F. Smet, C. Detavernier, and D. Poelman, "Stability of switchable SmS for piezoresistive applications," Nanotechnol. Mater. Devices Conf. NMDC 2016 - Conf. Proc., no. c, pp. 2–4, 2016, doi: 10.1109/NMDC.2016.7777086.

[9] A. Barla et al., "Pressure-Induced Magnetic Order in Golden SmS," Phys.

Rev. Lett., vol. 92, no. 6, pp. 1–4, 2004, doi: 10.1103/PhysRevLett.92.066401.

[10] F. De Tomasi, M. Rita, M. Lucia, and G. Leo, “Laser irradiation effects on the resistance of SmS films,” vol. 413, pp. 171–176, 2002.

[11] M. P. Petrov, A. I. Grachev, A. A. Kukharskii, I. A. Smirnov, and S. G. Shul’man, “Holographic storage in SmS thin films,” Opt. Commun., vol. 22, no. 3, pp. 293–296, 1977, doi: 10.1016/S0030-4018(97)90012-2.

[12] J. S. Meena, S. M. Sze, U. Chand, and T. Y. Tseng, “Overview of emerging nonvolatile memory technologies,” Nanoscale Res. Lett., vol. 9, no. 1, pp. 1–33, 2014, doi: 10.1186/1556-276X-9-526.

[13] N. Benbattouche, G.A. Saunders, and H. Bach, "The pressure and temperature dependences of the elastic properties of EuS", J. Phys. Chem. Solids, vol. 51, 181-188, 1990.

[14] V.L. Moruzzi, D.T. Teaney, "Specific heat of EuS", Solid State Commun., 1 (1963).

[15] K. Matsumoto et al., “Large magnetocaloric effect in sintered ferromagnetic EuS,” Cryogenics (Guildf)., vol. 79, pp. 45–48, 2016, doi: 10.1016/j.cryogenics.2016.08.001.

[16] V. A. Grazhulis, I. L. Bolotin, S. I. Bozhko, O. R. Bulanov, and A. M. Ionov, “Low-energy loss spectroscopy of compounds of family GdS_x (x = 0.8 - 1.25),” Surf. Sci., vol. 365, no. 3, pp. 748–752, 1996, doi: 10.1016/0039-6028(96)00778-9.

[17] V. A. Grazhulis, I. L. Bolotin, S. I. Bozhko, O. R. Bulanov, and A. M. Ionov, “Electronic structure of the valence band of GdS_x and Gd_3S_4,” Appl. Surf. Sci., vol. 104, pp. 68–72, 1996, doi: 10.1016/S0169-4332(96)00122-5.

[18] T. Bruckel et al., “Antiferromagnetic order and phase transitions in GdS as studied with X-ray resonance-exchange scattering,” Eur. Phys. J. B, vol. 19, no. 4, pp. 475–490, 2001, doi: 10.1007/s100510170293.

[19] L. N. Vasilev et al., “Physical properties and phase transitions of the rare

earth monosulphides in the homogeneity range," Phys. Status Solidi, vol. 80, no. 1, pp. 237–244, 1983, doi: 10.1002/pssa.2210800126.

[20] W. Beckenbaugh, J. Evers, G. Güntherodt, E. Kaldis, and P. Wachter, "Non-stoichiometric metals with strongly varying electron concentration: Gd-monochalcogenides and LaS," J. Phys. Chem. Solids, vol. 36, no. 4, pp. 239–248, 1975, doi: 10.1016/0022-3697(75)90016-5.

[21] S. mirnov I. A. Golubkov V., Goncharova E. V., Juze V. P., Loginov G. M., Sergeeva V. M., "Physical Properties of the Chalcogenides Rare-Earth Elements", Leningrad: Nauka,. 1973.

[22] F. Hulliger and M. L. and R. Schmelczer, "Low-Temperature Behavior of DyS, DySe, HoS and HoSe," Rare Earths Mod. Sci. Technol., vol. 3, pp. 455–456, 1982, doi: 10.1007/978-1-4613-3406-4.

[23] P. Fischer, W. Hälg, and F. Hulliger, "Magnetic ordering in HoBi, HoS, ErS and ErSe," Phys. B+C, vol. 130, no. 1–3, pp. 551–554, 1985, doi: 10.1016/0378-4363(85)90303-1.

[24] W. Beckenbaugh, G. Güntherodt, R. Hauger, E. Kaldis, and J. P. Kopp, "Magnetic Properties of Gadolinium Chalcogenides with Varying Stoichiometry," AIP Conf. Proc. 18, vol. 18, pp. 540–544, 1974, doi: 10.1063/1.3141770.

[25] Stephanie N. Gilbert Corder et al., "Near-field spectroscopic investigation of dual-band heavy fermion metamaterials," Nat. Commun., vol. 8, no. 2262, pp. 1–7, 2017, doi: 10.1038/s41467-017-02378-3.

[26] I. V. Golosovskii and V. P. Plakhty, "Magnetic Ordering in NdS," Phys. stat. sol., vol. 56, pp. 61–67, 1973.

[27] S. S. Aplesnin, A. M. Khar'Kov, M. N. Sitnikov, and V. V. Sokolov, "Spin reduction in the Mn1-xHoxS solid solutions," J. Magn. Magn. Mater., vol. 347, pp. 10–13, 2013, doi: 10.1016/j.jmmm.2013.07.044.

[28] "E. Bucher, A.C. Gonsard, K. Andres, 8th Intern. Rare Earth Research Conf. Reno USA (1970). Edit. T.A. Henrie, R.E. Lindstrom Reno, Nevada USA p.

174.,” p. 1970, 1970.

[29] G. A. Alanko and D. P. Butt, “Mechanochemical synthesis of cerium monosulfide,” J. Am. Ceram. Soc., vol. 97, no. 8, pp. 2357–2359, 2014, doi: 10.1111/jace.13018.

[30] Domange L., Flahaut J., Guittard M.; C. R. Acad. Sci. Paris 249 (1959) p697.

[31] Bach H., Erdt S., Stauche P.; J Cryst. Growth 62 (1983) p173 .

[32] Klemm, W., Senff, H., Z. Anorg. Chem, vol. 241(1939), p259.

[33] L. Li, S. Hirai, E. Nakamura, and H. Yuan, “Influences of Eu_2O_3characters and sulfurization conditions on the preparation of EuS and its large magnetocaloric effect,” J. Alloys Compd., vol. 687, pp. 413–420, 2016, doi: 10.1016/j.jallcom.2016.06.053.

[34] “E.D. Eastman, L. Brewer, L.A. Bromley, P.W. Gilles, and N.L. Lofgren, Preparation and Properties of the Sulfides of Thorium and Uranium,” J. Am. Chem. Soc., 72, (1950) 4019-23,” p. 4019, 1950.

[35] M. Guittard, C. R. Acad. Sci. Paris 261, p2109, (1965).

[36] G. G. Libowitz and J. G. Pack, “The Gadolinium-Hydrogen System at Elevated Temperatures. Vacancy interactions in gadolinium dihydride,” J. Phys. Chem., vol. 73, no. 7, pp. 2352–2356, 1969, doi: 10.1021/j100727a042.

[37] K. Fu et al., “Study on the thermodynamics of the gadolinium-hydrogen binary system (H/Gd = 0.0–2.0) and implications to metallic gadolinium purification,” J. Alloys Compd., vol. 673, pp. 131–137, 2016, doi: 10.1016/j.jallcom.2016.02.201.

[38] J. Flahaut, “Recherches récentes sur les sulfures métalliques,” Bull. Soc. Chim., pp. 1282–1290, 1960.

[39] S. Hirai et al., “Synthesis and Sintering of Cerium(III) Sulfide Powders,” J. Am. Ceram. Soc., vol. 81, no. 1, pp. 145–151, 1998, doi: 10.1111/j.1151-2916.1998.tb02306.x.

[40] J. Flahaut, M. Guittard, J. Toriers, and M. Partie, “Les sulfures et oxysulfures

de gadolinium, dysprosium et erbium," Compt. Rend., vol. 245, pp. 2291–2294, 1957.

[41] P. Peshev, "On the preparation and some physical properties of gadolinium sesquisulphide and gadolinium monosulphide," J. Less-Common Met., vol. 14, no. 4, pp. 379–386, 1968, doi: 10.1016/0022-5088(68)90161-6.

[42] J. A. Fries and E. D. Cater, "Vaporization, thermodynamics, and dissociation energy of gadolinium monosulfide: Systematics of vaporization of the rare earth monosulfides," J. Chem. Phys., vol. 68, pp. 3978–3989, 1978, doi: 10.1063/1.436311.

[43] K. Mattenberger, L. Scherrer, and O. Vogt, "Crystal growth of uranium monochalcogenides and monopnictides by mineralization in a special electron beam furnace," J. Cryst. Growth, vol. 67, no. 3, pp. 467–471, 1984, doi: 10.1016/0022-0248(84)90038-1.

[44] V. Parashar, S. K. Pandey, and A. C. Pandey, "Low-temperature synthesis of quantum size gadolinium monosulfide (GdS) nanoparticles and their pathogen capture efficiency.," Chem. Commun. (Camb)., vol. 46, no. 18, pp. 3143–5, 2010, doi: 10.1039/c000553c.

[45] P. Fischer, P. Schobinger-Papamantellos, E. Kaldis, and A. Ernst, "Magnetic ordering of rare earth monochalcogenides. II. Neutron diffraction investigation of terbium sulphide, telluride and holmium telluride," J. Phys. C Solid State Phys., vol. 10, no. 18, pp. 3601–3611, 1977, doi: 10.1088/0022-3719/10/18/024.

[46] M. Ohta, H. Yuan, S. Hirai, Y. Yajima, T. Nishimura, and K. Shimakage, "Thermoelectric properties of Th_3P_4-type rare-earth sulfides Ln_2S_3 (Ln = Gd, Tb) prepared by reaction of their oxides with CS_2 gas," J. Alloys Compd., vol. 451, no. 1–2, pp. 627–631, 2008, doi: 10.1016/j.jallcom.2007.04.078.

[47] H. Yuan, M. Ohta, S. Hirai, T. Nishimura, and K. Shimakage, "Preparation of terbium sesquisulfide and holmium sesquisulfide by sulfurization of their oxide powders using CS2 gas," Journal of Rare Earths, vol. 22, no. 6. pp. 759–762, 2004.

[48] M. Tokita, Spark Plasma Sintering (SPS) Method, Systems, and Applications, Second Edi. Elsevier Inc., 2013.

[49] W. Chen, U. Anselmi-Tamburini, J. E. Garay, J. R. Groza, and Z. A. Munir, "Fundamental investigations on the spark plasma sintering/synthesis process: I. Effect of dc pulsing on reactivity," Mater. Sci. Eng. A, vol. 394, no. 1–2, pp. 132–138, 2005, doi: 10.1016/j.msea.2004.11.020.

[50] M. Omori, "Sintering, consolidation, reaction and crystal growth by the spark plasma system (SPS)," Mater. Sci. Eng. A, vol. 287, no. 2, pp. 183–188, 2000, doi: 10.1016/s0921-5093(00)00773-5.

[51] N. Sato, M. Odori, M. Skrobian, M. Saito, T. Fujino, and N. Masuko, "Synthesis of Neodymium Sesquisulfide from Sulfate by Carbon Reduction.," Shigen-to-Sozai, vol. 110, no. 11, pp. 869–874, 1994, doi: 10.2473/shigentosozai.110.869.

[52] H. Yokokawa, S. Yamauchi, and T. Matsumoto, "Thermodynamic database MALT for windows with gem and CHD," Calphad Comput. Coupling Phase Diagrams Thermochem., vol. 26, no. 2, pp. 155–166, 2002, doi: 10.1016/S0364-5916(02)00032-9.

[53] T. N. Bien, S. Hirai, I. G. Vasilyeva, R. Nikolaev, C. Sekine, and K. Atsunori, "Study of non-stoichiometric GdS_x ($0.68 \leq x \leq 1.2$) processed by reaction sintering," J. Alloys Compd., vol. 831, p. 154691, 2020, doi: 10.1016/j.jallcom.2020.154691.

[54] E.K. Kasenas and D. M. Chizhikov, Pressure and the vapor composition under oxides of chemical elements, Nauka, Moskow 1976, 274. 1976.

[55] S. Hirai, E. Sumita, K. Shimakage, Y. Uemura, T. Nishimura, and M. Mitomo, "Synthesis and Sintering of Cerium(II) Monosulfide," J. Am. Ceram. Soc., vol. 87, no. 1, pp. 23–28, 2004, doi: 10.1111/j.1151-2916.2004.tb19939.x.

[56] C. A. Veliev, "Ho_2S_3-Ga_2S_3 phase diagram," Inorg. Mater., vol. 46, no. 5, pp. 452–455, 2010, doi: 10.1134/S002016851005002X.

[57] P. O. Andreev et al., “Temperatures and enthalpies of melting of Ln_2S_3 (Ln = Gd, Tb, Dy, Ho, Er, Tm, Yb, and Lu) compounds,” J. Therm. Anal. Calorim., vol. 131, no. 2, pp. 1545–1551, 2018, doi: 10.1007/s10973-017-6620-x.

[58] Y. I. Gibner and I. G. Vasilyeva, “Rapid heating in high-temperature thermomicroscopic analysis,” Journal of Thermal Analysis and Calorimetry, vol. 53, no. 1. pp. 151–160, 1998, doi: 10.1023/A:1010115620439.

[59] P. E. Nikolaev and I. G. Vasileva, “Vapor Pressure Determination for Solid and Liquid La_2S_3 using Boiling Points,” vol. 44, no. 12, pp. 1367–1371, 2008, doi: 10.1134/S0020168508120194.

[60] M. N. Abdusalyamova and I. G. Vasilyeva, “Phase equilibrium and intermediate phases in the Eu – Sb system,” J. Solid State Chem., vol. 184, pp. 2751–2755, 2011, doi: 10.1016/j.jssc.2011.08.018.

[61] V. V Bakovets, A. V Sotnikov, and I. V Korolkov, “Kinetics of phase formation in the Ln – O – S (Ln = La , Gd , Y) systems during oxide sul fi dation in ammonium thiocyanate vapor,” J. Am. Cerammic Soc., vol. 100, no. 4, pp. 1–10, 2017, doi: 10.1111/jace.14692.

[62] G. Bruzzon and G. L. Olcese, “Sur L’existence de solutions solides dans les sous-sulfures (MX) des terres rares,” Ed. CNRS Coll. Int., vol. 157, pp. 387–394, 1965.

[63] S. Bist, J. Kumar, and O. Srivastava, “On the existence and structure of gadolinium and samarium monoxides and their related lower oxides,” Phys. Status Solidi, vol. 197, pp. 197–206, 1972, doi: 10.1002/pssa.2210140124.

[64] E. Murad and D. L. Hildenbrand, “Dissociation energies of GdO, HoO, ErO, TmO, and LuO; correlation of results for the lanthanide monoxide series,” J. Chem. Phys., vol. 73, no. 8, pp. 4005–4011, 1980, doi: 10.1063/1.440627.

[65] G. B. and G. L. Ocese, “Sur L’existence de solutions solides dans les sous-sulfures (MX) des terres rares,” vol. 157, pp. 387–394, 1965.

[66] V. Khusnutdinova, V. S. Oskotspii, I. A. Smirnov, and V. M. Sergeeva,

"Thermal Conductivity of Gadolinium Monosulphide," Phys. Status Solidi, vol. 48, no. 1, pp. 353–357, 1971, doi: 10.1002/pssb.2220480134.

[67] F. Hulliger and T. Siegrist, "Low-Temperature Phase Transitions in GdS , GdSe and GdTe," Phase Transitions, vol. 90, pp. 81–90, 1979, doi: 10.1007/BF01322085.

[68] P. O. Andreeva and P. P. Fedorovb, "Phase diagrams of the systems Ln_2S_3-Ln_2O_3 (Ln = Gd, Dy)," Russ. J. Inorg. Chem., vol. 58, no. 6, pp. 724–727, 2013, doi: 10.1134/S0036023613060028.

[69] E. D. Eastman, L. Brewer, L. R. A. Bromley, P. W. Gilles, and N. L. Lofgren, "Preparation and Properties of Refractory Cerium Sulfides," J. Am. Chem. Soc., vol. 72, no. 5, pp. 2248–2250, 1950, doi: 10.1021/ja01161a102.

[70] B. Predel, Phase Equilibria, Crystallographic and Thermodynamic Data of Binary Alloys: Landolt-Bornstein, New Series, O. Madelung, ed., Springer, 5, 1991-1998. Subvol. (a) Dy-S, (b) La-S.

List of Publications

Journal Paper

1. **Tran Nhu Bien**, Shinji Hirai, Inga G. Vasilyeva, Ruslan Nikolaev, Chihiro Sekine, Atsunori Kamegawa, "*Study of non-stoichiometric GdS_x ($0.68 \leq x \leq 1.2$) processed by reaction sintering*," J. Alloys Compd., vol. 831, p. 154691, 2020, doi: 10.1016/j.jallcom.2020.154691.
2. **Tran Nhu Bien**, Shinji Hirai, Inga G. Vasilyeva, Ruslan Nikolaev, Chihiro Sekine, Atsunori Kamegawa, Kazuhei Wakiya, Yukihiro Kawamura "*Composition and microstructure of holmium monosulfide compacts processed by reaction sintering*," J. Alloys Compd., Available online 10 November, 2020, doi: 10.1016/j.jallcom.2020.157872.
3. Nikolaev R.E., Sulyaeva V.S., Alekseev A.V., Sukhikh A.S., Polyakova E.V., Pomelova T. A., Kuzuya T., Hirai S., **Tran Nhu B.**, Growth Mechanism of Helical γ-Dy_2S_3 Single Crystals, CrystEngComm, 2021, doi: 10.1039/D0CE01750G.

International Proceedings:

1. **Tran Nhu Bien,** Shinji Hirai et. al, "Synthesis of GdS_x ($0.68 \leq x \leq 1.2$) by Reaction Sintering in Pulse Electric Current Sintering Method and Its Properties," The 13 Pacific Rim Conference of Ceramic Societies, October 27, 2019 (Poster), Okinawa, Japan.

Proceedings of Local Presentation:

1. **Tran Nhu Bien,** Shinji Hirai et. al, "Synthesis of Light Rare Earth Sesquisulphides Utilizing Phase Transformation Induced by the Addition of Titanium", Muroran-IT Rare Earth Workshop, October 2017, Kasumigaseki-Tokyo, Japan
2. **Tran Nhu Bien**, Shinji Hirai et. al, "Preparation of GdS by Reaction Sintering in Pulse Electric Current Sintering Method", Muroran-IT Rare Earth Workshop, November 2018, Toyako-Hokkaido, Japan